

RESEARCH ARTICLE

Interplay between actomyosin and E-cadherin dynamics regulates cell shape in the *Drosophila* embryonic epidermis

Joshua Greig and Natalia A. Bulgakova*

ABSTRACT

Precise regulation of cell shape is vital for building functional tissues. Here, we study the mechanisms that lead to the formation of highly elongated anisotropic epithelial cells in the *Drosophila* epidermis. We demonstrate that this cell shape is the result of two counteracting mechanisms at the cell surface that regulate the degree of elongation: actomyosin, which inhibits cell elongation downstream of RhoA (Rho1 in *Drosophila*) and intercellular adhesion, modulated via clathrin-mediated endocytosis of E-cadherin (encoded by *shotgun* in flies), which promotes cell elongation downstream of the GTPase Arf1 (Arf79F in *Drosophila*). We show that these two mechanisms do not act independently but are interconnected, with RhoA signalling reducing Arf1 recruitment to the plasma membrane. Additionally, cell adhesion itself regulates both mechanisms – p120-catenin, a regulator of intercellular adhesion, promotes the activity of both Arf1 and RhoA. Altogether, we uncover a complex network of interactions between cell–cell adhesion, the endocytic machinery and the actomyosin cortex, and demonstrate how this network regulates cell shape in an epithelial tissue *in vivo*.

KEY WORDS: Cell shape, Epithelium, Adhesion, Actin, p120ctn

INTRODUCTION

The morphogenesis of all tissues requires precise control over the shape of individual cells. In epithelia, which outlines all cavities and surfaces of animal bodies, a variety of cell shapes is observed. Cell shape is determined by mechanical properties, which define cell geometry based on intracellular and intercellular forces (Chalut and Paluch, 2016; Lecuit and Lenne, 2007). At the cell surface, mechanical properties are determined by an interplay of two factors: cortical actin and intercellular adhesion (Lecuit and Lenne, 2007; Winklbauer, 2015).

The first factor, cortical actin, is a meshwork of actin filaments crosslinked by specific crosslinking proteins and myosin motors at the cell surface (Chugh and Paluch, 2018). Cortical tension is predominantly generated by the activity of non-muscle Myosin II (MyoII) motors, which act to minimise the contact area between cells by pulling on actin filaments, although the architecture of these filaments also contributes to tension regulation (Blankenship et al., 2006; Chugh et al., 2017; Clark et al., 2014). One of the best documented regulators of cortical contractility is the GTPase RhoA (Rho1 in *Drosophila*; Spiering and Hodgson, 2011). Its key effector

is the enzyme Rho kinase (Rok), which is recruited to membranes by the activated form of RhoA, where it phosphorylates myosin light chain, leading to activation of MyoII and an increase in actin contractility (Amano et al., 2010; Kawano et al., 1999; Kureishi et al., 1997; Leung et al., 1995).

The second factor, intercellular adhesion, is the property of one cell binding to its neighbours using specialised proteins on its surface. In epithelia, this is mediated by adherens junctions (AJs), with E-cadherin (E-cad; encoded by *shotgun* in *Drosophila*) being the principal component. This transmembrane protein binds to E-cad molecules on adjacent cells (Takeichi, 1977; van Roy and Berx, 2008). Intercellular adhesion often opposes cortical tension by increasing the contact surface between cells (De Vries et al., 2004; Lecuit and Lenne, 2007), and its strength is proportional to both the levels and dynamics of E-cad at the cell surface (Foty and Steinberg, 2005; Troyanovsky et al., 2006). The latter largely relies on the processes of endocytosis and recycling, which constantly remodel AJs (Kowalczyk and Nanes, 2012).

The p120-catenin (p120ctn) protein family are the key regulators of E-cad endocytosis in mammalian cells, through directly binding the juxtamembrane domain of E-cad (Daniel and Reynolds, 1995; Garrett et al., 2017; Ireton et al., 2002; Oas et al., 2013; Shibamoto et al., 1995; Yap et al., 1998; Yu et al., 2016). This family is represented by a single gene in invertebrates, such as *Drosophila*, whereas humans have seven members with different expression patterns and functional requirements (Carnahan et al., 2010; Gul et al., 2017; Hatzfeld, 2005). Most studies have focused on the founding family member, p120ctn (encoded by *CTNND1* in mammals); however, other members, δ -catenin (*CTNND2*) and ARVCF, seem to have similar functions (Davis et al., 2003). In mammalian cells, p120ctn is required to maintain E-cad at the plasma membrane – uncoupling p120ctn from E-cad or reducing expression results in complete internalisation of E-cad (Davis et al., 2003; Ireton et al., 2002; Ishiyama et al., 2010), as the binding of p120ctn to E-cad conceals endocytosis-triggering motifs (Nanes et al., 2012; Reynolds, 2007). This model of p120ctn activity has recently been augmented, when it was found that p120ctn can also promote endocytosis of E-cad through interaction with Numb (Sato et al., 2011).

By contrast, in *Drosophila* and *C. elegans*, p120ctn was thought to play only a supporting role in adhesion, because genetic ablation failed to replicate the effects observed in mammalian systems (Myster et al., 2003; Pacquelet et al., 2003; Pettitt et al., 2003). This was thought to be due to the greater similarity of invertebrate p120ctn to mammalian δ -catenin, ablation of which is similarly viable in mice (Carnahan et al., 2010; Israely et al., 2004). However, δ -catenin expression is restricted to neural and neuroendocrine tissues (Ho et al., 2000), which is likely to explain the mildness of knockout phenotypes, whereas invertebrate p120ctn is broadly expressed in both epithelia and neurons (Myster et al., 2003), suggesting potential functional similarity with mammalian p120ctn, which shares the broad expression pattern (Davis et al., 2003). It has recently been reported that *Drosophila* p120ctn is required to stabilise E-cad in the

Department of Biomedical Science and Bateson Centre, The University of Sheffield, Sheffield S10 2TN, UK.

*Author for correspondence (n.bulgakova@sheffield.ac.uk)

DOI: 10.1242/jcs.242321; J.G., 0000-0001-9742-7438; N.A.B., 0000-0002-3780-8164

Handling Editor: Kathleen Green

Received 28 November 2019; Accepted 1 July 2020

pupal wing (Iyer et al., 2019) and promotes the endocytosis and recycling of E-cad in the embryo and larval wing discs (Bulgakova and Brown, 2016). This indicates an evolutionary conservation of p120ctn function where, depending upon the context, p120ctn either inhibits or promotes E-cad endocytosis.

Another protein family regulating E-cad endocytosis is the Arf GTPases, which recruit coat proteins to facilitate intracellular trafficking (Donaldson and Jackson, 2011). The first family member, Arf1 (also known as Arf79F in *Drosophila*), is classically viewed as Golgi resident and responsible for anterograde transport from the Golgi to the plasma membrane (Donaldson and Jackson, 2011; McMahon and Boucrot, 2011). Recently, however, Arf1 was detected at the plasma membrane, where it co-operates with Arf6-dependent endocytosis (Humphreys et al., 2013; Padovani et al., 2014). In *Drosophila*, Arf1 is required for endocytosis in the early syncytial embryo (Humphreys et al., 2012; Lee and Harris, 2013; Rodrigues et al., 2016), and interacts with E-cad and another component of AJs, Par-3 (Bazooka in *Drosophila*) (Shao et al., 2010; Toret et al., 2014).

Cortical actin and intercellular adhesion do not exist in isolation but are intimately interconnected. Intracellularly E-cad interacts with other catenin proteins: E-cad binds β -catenin (encoded by *armadillo*), with α -catenin binding β -catenin and actin, thus directly linking E-cad to cortical actin (Ozawa et al., 1990; Shapiro and Weis, 2009). In addition to direct linkage, cortical actin and intercellular adhesion share common regulators. In mammalian epithelial cells, RhoA localises to AJs, where E-cad complexes create local zones of active RhoA by recruiting the Ect2 guanine-nucleotide-exchange factor (GEF) through α -catenin (Priya et al., 2013; Ratheesh et al., 2012). In these cells, p120ctn has a context-dependent role in RhoA regulation: it can inhibit RhoA directly or indirectly via the GTPase-activating protein (GAP) p190RhoGAP, direct its spatiotemporal activity, or activate it (Anastasiadis et al., 2000; Derksen and van de Ven, 2017; Lang et al., 2014; Taulet et al., 2009; Yu et al., 2016; Zebda et al., 2013). The role of p120ctn in the RhoA pathway in *Drosophila* is unclear (Fox et al., 2005; Magie et al., 2002). However, RhoA itself regulates E-cad and is required for establishment of E-cad-mediated adhesion (Braga et al., 1997). In *Drosophila*, RhoA promotes the regulated endocytosis of E-cad by Dia and AP2 (Levayer et al., 2011). Conversely, RhoA activity antagonises E-cad endocytosis in the early embryo (Lee and Harris, 2013), indicating a context-dependent role of RhoA in E-cad endocytosis. Furthermore, E-cad endocytosis can direct actin remodelling (Hunter et al., 2015).

Here, we investigated the interplay between cortical actin, specifically actomyosin, and E-cad-mediated adhesion in the elongated cells of the late embryonic epidermis in *Drosophila*. This cellular elongation is accompanied by a reciprocal anisotropy of cortical tension and E-cad adhesion. p120ctn is directly involved in shaping these cells by both influencing the endocytosis of E-cad and modulating cortical tension. We found that the mechanism of this p120ctn dual function is dependent on interactions with two GTPase pathways: RhoA, to increase cortical tension and inhibit endocytosis; and Arf1, to promote endocytosis. Finally, we show that the interplay between these two GTPase pathways downstream of p120ctn participates in shaping the morphology of cells *in vivo*.

RESULTS

Anisotropy of actomyosin and adhesion in the epidermis of stage 15 *Drosophila* embryos

The epidermal cells of stage 15 *Drosophila* embryos are elongated in the direction of the dorsal–ventral embryo axis and have an average aspect ratio of 6.1 ± 1.3 (ratio between lengths of the long

and short cell axes, $\text{mean} \pm \text{s.d.}$; Fig. 1A–E). Consistent with the elongated shape, these cells have two distinct types of cell border: long borders, which are orthogonal to the anterior–posterior axis of the embryo (AP borders), and short borders, which are orthogonal to the dorsal–ventral axis (DV borders; Fig. 1B–D').

These cells exhibit an asymmetric distribution of intercellular adhesion components, specifically, the levels and dynamics of E-cad. In these differentiated cells, E-cad localises asymmetrically with a 1:2 AP:DV ratio (Fig. 1F; Table S1; Bulgakova et al., 2013) in a narrow continuous band of mature AJs (Adams et al., 1996; Tepass and Hartenstein, 1994). This asymmetry is due to an accumulation at the DV borders of a specific pool of E-cad, which is dynamic due to its endocytic trafficking (Bulgakova et al., 2013).

Further to the asymmetry of E-cad, cortical tension and MyoII are also anisotropic between the AP and DV borders. MyoII–YFP (*Drosophila* Zipper fused with YFP) is enriched at the AP borders (AP:DV of $\sim 2:1$; Fig. 1G,H; Table S1), consistent with previous reports (Bulgakova et al., 2013; Simoes et al., 2010). As the accumulation of MyoII has been linked to cortical tension (Priya et al., 2015; Scarpa et al., 2018; Yu and Fernandez-Gonzalez, 2016), we compared tension between the AP and DV borders using microablation and measured the initial recoil, which is proportional to the tension (Liang et al., 2016; Mao et al., 2013). We used an E-cad tagged at its endogenous locus (E-cad–GFP, Huang et al., 2009) to label cells and quantify recoil (Fig. 1I–K; Movies 1, 2). The initial recoil was positive for the AP borders, showing that they are under tension, and negative for the DV borders, suggesting that they are under compression (Fig. 1J). Intriguingly, the initial reduction in the distance between the vertices of the DV borders was followed by expansion that exceeded the original border length (Fig. 1K).

Overall, the elongated shape of these epidermal cells coincides with inverse anisotropies in actomyosin-dependent tension and the levels and dynamics of adhesion complexes. Therefore, we investigated how the interplay between cortical tension and adhesion at the cell surface produces cell shape.

p120ctn influences cell shape, RhoA signalling and cortical tension

Members of the p120ctn family regulate both the actin cytoskeleton and cadherin trafficking and are thus good candidates to mediate their interplay. We investigated whether the function of p120ctn, with only one family member in *Drosophila*, affected the shape of cells. We overexpressed p120ctn under the control of a *UAS* promoter (*UAS::p120ctn*) in the posterior half of each embryonic segment using the *engrailed::GAL4* (*en::GAL4*) driver while marking the cells using *UAS::CD8–Cherry* (Fig. 2A). To exclude potential differences between the compartments we used an external control: an *engrailed* compartment expressing two copies of *UAS::CD8–Cherry* to balance the *Gal4:UAS* ratio (Fig. 2A). The cells expressing *UAS::p120ctn* appeared distorted and had a reduced aspect ratio ($P < 0.0001$; Fig. 2A,B). We complemented this analysis by using a *p120ctn* mutant (Fig. 2A; Bulgakova and Brown, 2016). Unexpectedly, the loss of p120ctn also reduced the cell aspect ratio in the *engrailed* compartment ($P = 0.001$; Fig. 2C,D). This differs from the previous report (Bulgakova and Brown, 2016), which can be attributed to inherent differences between the *engrailed*-positive and -negative compartments (Fig. S1A). This difference was not accounted for in the previous report and is likely to mask the effect of p120ctn depletion. Therefore, altering the levels of p120ctn changes elongation of cells in the *Drosophila* epidermis.

Another regulator of cell shape is cortical actomyosin, which is influenced by RhoA signalling. Because p120ctn family members

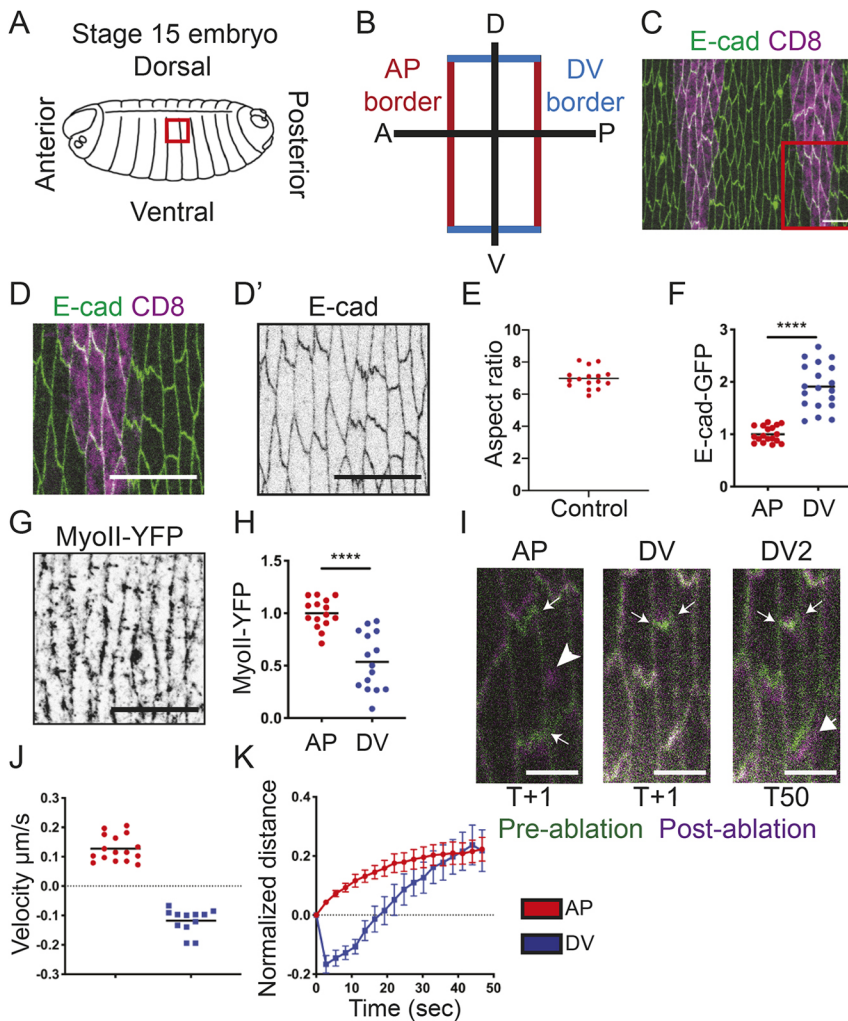


Fig. 1. Cell anisotropy of the stage 15 *Drosophila* embryonic epidermis. (A–D) Overview of the stage 15 *Drosophila* embryo. (A) Diagram of a stage 15 *Drosophila* embryo. Dorsolateral epidermis is indicated by a red box. (B) Schematic of the two cell borders: the longer anterior–posterior border (AP, red) and the shorter dorsal–ventral border (DV, blue). (C) Apical view of the epidermal region highlighted by the red box in A. Cells are outlined by E-cad–GFP (green), the *engrailed* compartment is marked by UAS::CD8–Cherry (magenta). Red box indicates the region shown magnified in D and D'. (D, D') Magnified image of the region highlighted in C, displayed as two colour (D) or single channel (D', E-cad–GFP in grey). (E) Aspect ratio of cells and (F) amounts of E-cad–GFP at the AP and DV cell borders in embryos expressing only E-cad–GFP. (G) MyoII–YFP in the same plane as E-cad. (H) Amounts of MyoII–YFP at the cell borders in control embryos. (I) Laser ablation of AP border (left panel) and a DV border (middle and right panels) in epidermal cells of embryos expressing E-cad–GFP in an otherwise wild-type background. Image is an overlay of pre-ablation (green) and post-ablation (magenta). The small arrows indicate the connected vertices of the ablated membrane used to measure initial recoil. Large arrow in the left panel shows the area of ablation, large arrow in the right panel indicates AP displacement late in DV ablation experiment (time, T, in seconds, T+1 is immediately post-ablation, T50 is the endpoint). (J) The initial recoil of the AP and DV membranes. (K) Time series of the ablation experiment measuring distance between vertices. Statistical analysis used a two-tailed Student's *t*-test with Welch's correction. All membrane intensity and ablation data are in Table S1. **** $P < 0.0001$. Each dot represents an individual embryo, with means indicated by horizontal lines. For intensity measurements, $n = 10$ –20 embryos per genotype with a minimum of 27 cells imaged per embryo. For ablation two junctions per border were averaged to give a mean value per embryo. Data in K are mean \pm s.e.m. Scale bars: 10 μ m (C,D,G); 5 μ m (I).

regulate RhoA signalling, we examined the interaction between p120ctn and RhoA in our system using its downstream target, non-muscle MyoII. p120ctn overexpression increased the amount of MyoII–YFP at the AP borders ($P = 0.006$; Fig. 2E,F). Conversely, in the p120ctn mutant embryos MyoII–YFP levels were reduced at the AP borders ($P = 0.01$; Fig. 2G,H). The levels of MyoII–YFP at the DV borders were not affected in either case ($P = 0.47$ and $P = 0.45$; Fig. 2F,H). We complemented these experiments by using a tagged kinase-dead variant of Rok (Rok^{KD}–Venus; Simoes et al., 2010), previously used as a readout of Rok localisation and activity (Bulgakova et al., 2013; Simoes et al., 2010), and a biosensor of RhoA activity – the RhoAGTP-binding domain of anillin (RBD–GFP; Munjal et al., 2015) to directly examine RhoA activation. Both Rok^{KD}–Venus and RBD–GFP had the same localisation and were affected in the same manner as MyoII–YFP (Fig. S1B–G). Overexpression of p120ctn led to elevated Rok^{KD}–Venus and RBD–GFP at the AP borders ($P = 0.0043$ and $P = 0.08$, respectively; Fig. S1B,C,F,G), whereas p120ctn loss abolished Rok^{KD}–Venus asymmetry due to a reduction at the AP borders ($P = 0.013$; Fig. S1D,E). These findings support that these three readouts can be used interchangeably. As a control we also measured total F-actin using LifeAct–GFP (Riedl et al., 2008), and found that it localised symmetrically and was not affected by altered p120ctn levels ($P > 0.99$, $P = 0.63$; Fig. S1H,I). These results indicated that p120ctn activates RhoA signalling specifically at the AP borders in a dose-dependent manner in epidermal cells.

Because of this correlation between p120ctn levels and RhoA signalling on the AP cell borders, we measured the cortical tension at these borders in p120ctn overexpressing and mutant cells (Fig. 2I–K; Movies 1, 3 and 4). Overexpression of p120ctn increased both the total recoil distance and the initial recoil velocity (0.36 μ m/s in comparison to 0.13 μ m/s, $P < 0.0001$; Fig. 2J,K). Conversely, in p120ctn mutant cells both the total recoil distance and initial velocity (0.07 μ m/s) were decreased ($P = 0.022$; Fig. 2J,K). This demonstrated that cortical tension correlates with p120ctn levels.

Overall, the changes in p120ctn levels altered the shape of epidermal cells, with the levels of p120ctn positively correlating with the activity of RhoA signalling and cortical tension at the AP borders. The DV borders displayed no change in the activity of RhoA signalling, indicating an anisotropic action of p120ctn.

p120ctn regulates the amount and dynamics of E-cad within adhesion sites

The other factor that contributes to cell shape is intercellular adhesion. p120ctn binds to the intracellular domain of E-cad, which regulates its endocytosis (Bulgakova and Brown, 2016; Iyer et al., 2019; Nanes et al., 2012; Reynolds, 2007; Sato et al., 2011). Using a ubiquitously expressed p120ctn tagged with GFP (*Ubi::p120ctn*–GFP), we determined that p120ctn colocalised with E-cad, mimicking its localisation with an enrichment at the DV borders ($r = 0.868$, $P < 0.00001$; Fig. 3A–C). Note that in this system, the antibody against the N-terminus of p120ctn fails to reproduce the

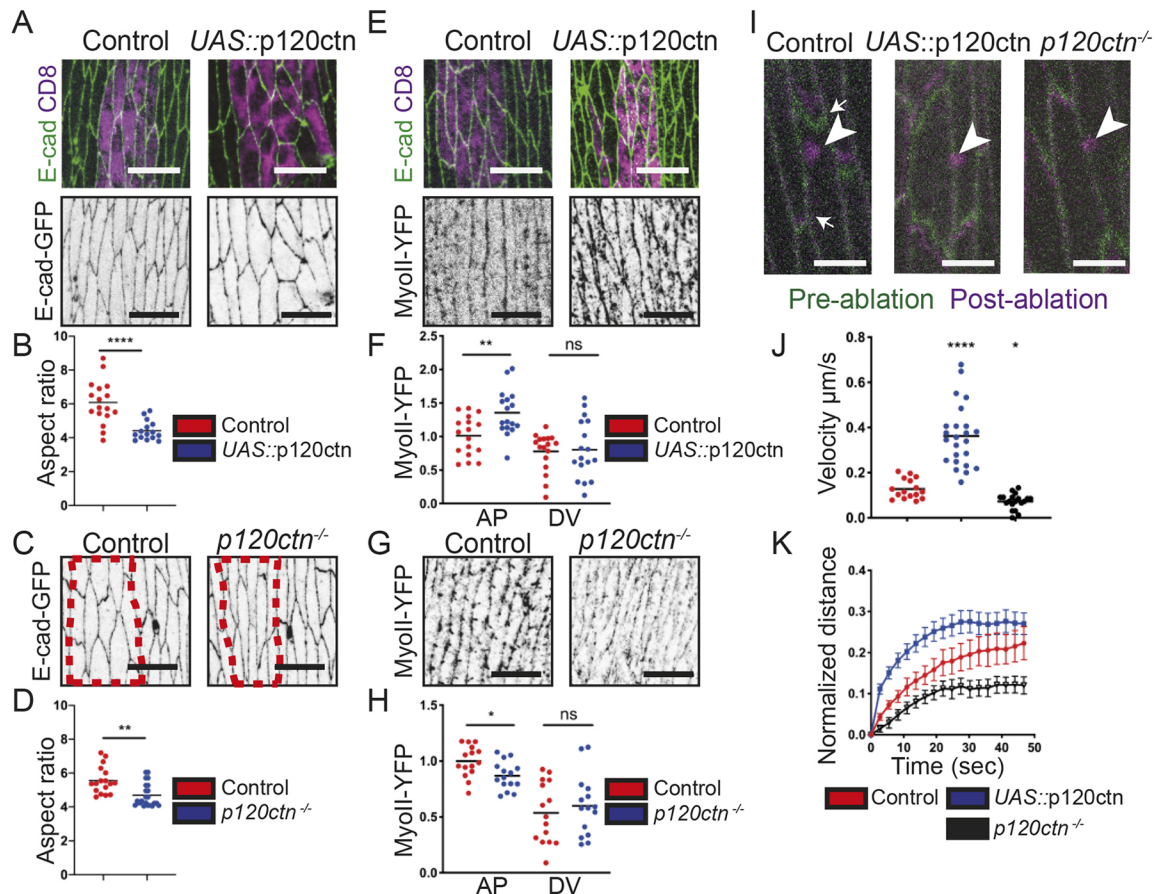


Fig. 2. p120ctn levels affect cell shape, actomyosin and cortical tension. (A) Apical views of epidermis expressing *UAS::CD8–Cherry* (left) and co-expressing it with *UAS::p120ctn* (right) using *en::GAL4* with E-cad–GFP (green, top; grey, bottom) and *UAS::CD8–Cherry* (magenta). (B) Aspect ratio of the control (*UAS::CD8–Cherry*) and *UAS::p120ctn*-expressing cells. (C) Control and *p120ctn*^{−/−} mutant epidermal cells marked by E-cad–GFP (grey). *engrailed*-positive cells are outlined (red). (D) Aspect ratio of control and *p120ctn*^{−/−} mutant cells. (E) Apical views of epidermis expressing MyoII–YFP (grey, bottom) in control expressing *UAS::CD8–Cherry* (left) or co-expressing it with *UAS::p120ctn* (right) using *en::GAL4* (magenta, top). Cell outlines are visualised using E-cad antibody (green, top). (F) Levels of MyoII–YFP at both cell borders in *p120ctn* overexpressing embryos. (G) MyoII–YFP (grey) in control and *p120ctn*^{−/−} mutant cells. (H) MyoII–YFP levels in control and *p120ctn*^{−/−} mutant cells. Scale bars: 10 μ m. (I) Laser ablation of AP cell borders in control (left), *p120ctn* overexpression (middle) and *p120ctn*^{−/−} mutant (right) cells. Images are an overlay of pre-ablation (green) and post-ablation (magenta). The small arrows indicate the connected vertices of the ablated membrane used to measure recoil. The large arrows represent the position of microablation. Scale bars: 5 μ m. (J) The initial recoil velocity of the membranes in the three genotypes. (K) Time series of the ablation experiment measuring distance between vertices. Statistical analysis was done using a two-way ANOVA (difference between cell borders) or a two-tailed Student's *t*-test with Welch's correction (aspect ratio and laser ablation). All best-fit and membrane intensity data are in Table S1. ns, not significant; **P*<0.05; ***P*<0.01; *****P*<0.0001. Each dot represents an individual embryo, with means indicated by horizontal lines. *n*=10–20 embryos per genotype with a minimum of 24 cells imaged per embryo. For ablation two junctions per embryo were averaged to give a mean value per embryo. Data in K are mean±s.e.m.

localisation of the full-length GFP-tagged p120ctn (Fig. S2A). Given this colocalisation, we examined whether changes in E-cad levels were observed when the levels of p120ctn were altered. Overexpression of p120ctn increased E-cad–GFP levels at both AP and DV borders (*P*<0.0001 and *P*=0.023, respectively; Fig. 3D,E, see also Fig. 2A). Conversely, the loss of p120ctn resulted in an isotropic decrease in E-cad–GFP at AP and DV borders (*P*=0.008 and *P*=0.035, respectively; Fig. 3F,G).

Next, we overexpressed p120ctn–GFP (*UAS::p120ctn*–GFP) driven by *en::GAL4* to compare p120ctn and E-cad localisation in the same cell. We detected an AP:DV ratio of 2:3 for both E-cad and p120ctn (Fig. 3H–J). The lower than usual AP:DV ratio of E-cad was similar to that observed when untagged p120ctn was overexpressed. As this E-cad distribution was identical to the distribution of p120ctn itself, we concluded that additional E-cad molecules are recruited as a protein complex with p120ctn.

The strength of cell adhesion and the number of adhesion complexes are regulated by endocytosis, and p120ctn has been

shown to inhibit and promote E-cad endocytosis in mammalian and *Drosophila* cells (Bulgakova and Brown, 2016; Ireton et al., 2002; Nanes et al., 2012; Sato et al., 2011; Xiao et al., 2003). Therefore, we used fluorescence recovery after photobleaching (FRAP), which reveals the stable fraction of the protein (which does not exchange on the timescale of the experiment) and the mobile fraction. The E-cad–GFP mobile fraction was 70% for DV borders and 60% for AP borders in control cells, with 30% and 40% of protein being immobile, respectively (Fig. 3K–M; for best-fit data see Table S1).

E-cad–GFP was less dynamic at both border types in p120ctn overexpressing cells (Fig. 3K–M). The immobile fractions were approximately 60% and 50% for AP and DV borders, respectively, which resulted in a decrease of the mobile fraction to 40% and 50% (*P*=0.0023 and *P*<0.0001 relative to control, respectively; Table S1). This is similar to the changes in the dynamics of E-cad–GFP in *p120ctn* mutants, where an increase in the immobile E-cad–GFP fraction is also observed (Fig. S2B–D; Bulgakova and Brown, 2016). Therefore, although p120ctn levels correlate with the levels E-cad at

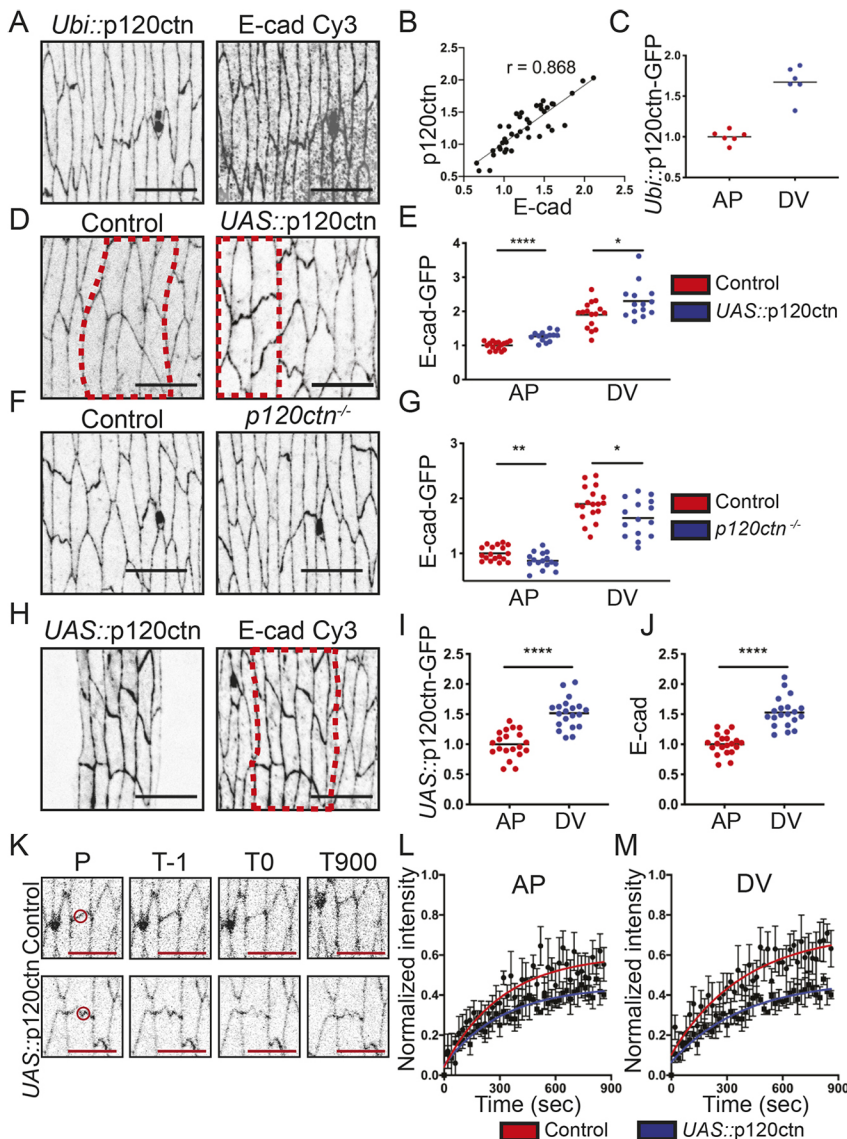


Fig. 3. p120ctn regulates both the levels and dynamics of E-cad. (A) Apical view of epidermal cells expressing a *Ubi::p120ctn*–GFP with cell borders visualised by the transgene itself (grey, left) and stained with an anti-E-cad antibody (grey, right). (B) Pearson's correlation of the signal intensities between E-cad and *Ubi::p120ctn*–GFP. (C) Levels of *Ubi::p120ctn*–GFP. (D,E) Apical views (D) and levels of E-cad–GFP (E) in embryos overexpressing *UAS::p120ctn*. (F,G) Apical views (F) and levels of E-cad–GFP (G) in epidermis of control and *p120ctn*^{−/−} mutant embryos. (H) Localisation of *UAS::p120ctn*–GFP (left) and E-cad (visualised using anti-E-cad antibody, right). (I,J) Quantification of levels of *UAS::p120ctn*–GFP (I) and E-cad (J) in *UAS::p120ctn*–GFP expressing cells. (K–M) Dynamics of E-cad–GFP measured by FRAP. Representative examples (K) and quantification (L,M) of E-cad–GFP FRAP in control and *UAS::p120ctn*–expressing cells. Panels in K show the DV cell border region bleached (position P, red circle) at the pre-bleach (time T−1), bleach (time T0) and the end (time T900) timepoints. Time is in seconds. Average recovery curves (mean±s.e.m.) and the best-fit curves (solid lines) are shown in L,M. Red dashed lines indicate the outlines of *engrailed*-positive cells in D and H. All best-fit and membrane intensity data are in Table S1. Statistical analysis was done using two-way ANOVA or a two-tailed Student's *t*-test with Welch's correction. **P*<0.05, ***P*<0.01, *****P*<0.0001. Each dot represents an individual embryo, with means indicated by horizontal lines. *n*=10–20 embryos per genotype with a minimum of 24 cells imaged per embryo. For FRAP, 8–10 embryos were used, with two AP and DV cell borders measured and averaged per embryo. Scale bars: 10 μm (A,D,F,H); 5 μm (K).

the plasma membrane, both the overexpression and loss of p120ctn lead to an increase of the immobile E-cad fraction. Next, we sought to determine the mechanism of these changes in E-cad dynamics and how they contribute to cell shape.

p120ctn and RhoA regulate E-cad via clathrin-mediated endocytosis

To ascertain whether the increase in immobile E-cad–GFP in response to altered p120ctn levels was due to an impairment of endocytosis, we examined clathrin. We used Clathrin light chain (CLC) tagged with GFP (*UAS::CLC*–GFP, Loerke et al., 2005; Wu et al., 2001b), to monitor clathrin behaviour in the plane of AJs by performing FRAP (Fig. 4A–C). CLC–GFP incorporates functionally into clathrin-coated pits (Chang et al., 2002; Gaidarov et al., 1999; Kochubey et al., 2006), and its recovery in FRAP reflects endocytic dynamics: in HeLa cells, the immobile fraction of CLC–GFP increases upon downregulation of endocytosis (Wu et al., 2001a). CLC–GFP expressed using *en::GAL4* was found in spots on the plasma membrane in the plane of AJs and in the cytoplasm (Fig. 4A), a localisation consistent with its function (Kaksonen and Roux, 2018). p120ctn overexpression reduced the mobile fraction of CLC–GFP by 30% (*P*<0.0001; Fig. 4C,D). A similar reduction in

CLC–GFP mobile fraction by 25% was found in *p120ctn* mutants (*P*<0.0001; Fig. 4C,E). These reflect the changes observed in E-cad FRAP, suggesting that CLC–GFP recovery is a valid proxy for E-cad dynamics in these cells.

Because p120ctn overexpression resulted in anisotropic activation of RhoA signalling, we asked whether this alone was responsible for the changes in E-cad. We directly inhibited the RhoA pathway using dominant negative RhoA (RhoA^{DN}). RhoA^{DN}, expressed constitutively using *en::GAL4*, resulted in a complete loss of E-cad at the membrane by stage 15 of embryogenesis. Therefore, we acutely induced the expression of the RhoA^{DN} using ubiquitously expressed temperature sensitive *GAL80^{ts}* and a temperature shift for 4 h at 12 h after egg laying (Pilauri et al., 2005). This acute downregulation reduced the amounts of E-cad–GFP at the AP borders (*P*=0.0078; Fig. 4F,G). Note that in this case E-cad asymmetry was reduced in control cells, likely due to the effects of the temperature shift. Due to the punctate pattern of E-cad–GFP potentially affecting the average intensity measurements, we also measured the total protein on the plasma membrane. We found reduced E-cad–GFP total protein content following the acute downregulation of RhoA (*P*<0.0001; Fig. S2H).

In a complementary experiment, we expressed a constitutively active RhoA^{CA} to elevate RhoA signalling directly (Fig. 4H). The

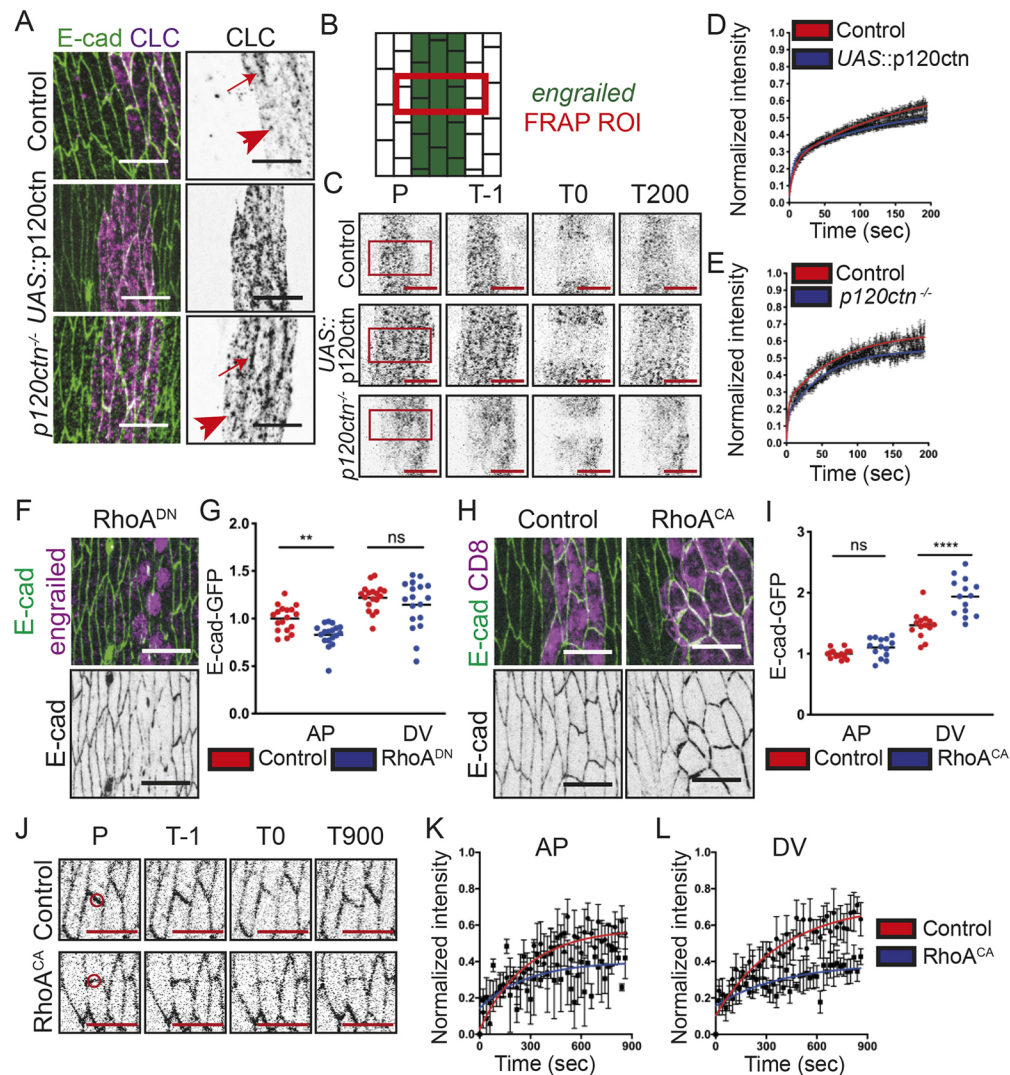


Fig. 4. p120ctn and RhoA change the dynamics of clathrin-mediated endocytosis. (A–E) The localisation and dynamics of UAS::CLC–GFP in control, p120ctn overexpressing (UAS::p120ctn) and p120ctn^{−/−} mutant embryos. (A) Distinct CLC–GFP puncta (magenta in left panels and black in right panels, examples indicated with red arrows) are observed at the membrane and in the cytoplasm. Cell outlines are visualised using anti-E-cad antibody (green, left). (B) Schematic of FRAP experiments: green cells, the *engrailed* compartment, which expresses transgenes; red box, the region bleached, encompassing an area spanning the compartment in a single z-plane in the middle of the AJ. (C–E) Representative examples (C) and quantification (D,E) of CLC–GFP FRAP in control, UAS::p120ctn and p120ctn^{−/−} mutant cells. Panels in C show the region bleached (position P, red box) at the pre-bleach (time T−1), bleach (time T0), and the end (time T200) timepoints. (F,G) Representative example (F) and levels (G) of E-cad–GFP in cells expressing RhoA^{DN} for 4 h compared to internal control. Cells expressing transgenes are marked with an antibody for Engrailed (magenta). (H,I) Representative examples (H) and levels (I) of E-cad–GFP in RhoA^{CA}-expressing cells. (J–L) Representative examples (J) and quantification (K,L) of E-cad–GFP FRAP in control and RhoA^{CA}-expressing cells. Panels in J show the DV cell border region bleached (position P, red circle) at the pre-bleach (time T−1), bleach (time T0) and the end (time T900) timepoints. Time in C and J is in seconds. Average recovery curves (mean±s.e.m.) and the best-fit curves (solid lines) are shown in D, E, K and L. All best-fit and membrane intensity data are in Table S1. Statistical analysis was done using two-way ANOVA or a two-tailed Student's *t*-test with Welch's correction. ns, not significant; ***P*<0.01; *****P*<0.0001. Each dot represents an individual embryo, with means indicated by horizontal lines. *n*=10–20 embryos per genotype with a minimum of 24 cells imaged per embryo. For FRAP, 8–10 embryos were used, with a single rectangular band encompassing an *engrailed* stripe used per embryo for UAS::CLC–GFP, and with two AP and DV cell borders measured and averaged per embryo for E-cad–GFP. Scale bars: 10 μm (A,C,F,H); 5 μm (J).

expression of RhoA^{CA} increased the amounts of E-cad–GFP, specifically at the DV but not the AP borders (*P*<0.0001 and *P*=0.34, respectively; Fig. 4I), consistent with an ectopic activation of RhoA signalling at the DV borders. We then asked whether this increase could be explained by a larger immobile fraction of E-cad–GFP. Using FRAP, we observed a significant increase in the immobile fraction of E-cad–GFP at both the AP and DV borders (*P*=0.02 and *P*<0.0001, respectively; Fig. 4J–L). To further explore whether this increase in the immobile E-cad was linked to clathrin-mediated endocytosis, we measured the dynamics of clathrin in the

plane of AJs using FRAP. Indeed, the mobile fraction of CLC–GFP was reduced by 40% (*P*<0.0001; Fig. S2E–G). This finding was consistent with the increase of both E-cad levels and immobile fraction in cells overexpressing the RhoA activator RhoGEF2, and the opposite effect upon RhoGEF2 downregulation (Bulgakova et al., 2013).

Overall, these data suggest that p120ctn leads to an activation of RhoA signalling at the AP borders, which increases both the total amount and immobile fraction of E-cad at these borders, most likely by preventing E-cad endocytosis.

Localisation of the GTPase Arf1 at the plasma membrane depends on p120ctn and RhoA, and promotes clathrin-mediated endocytosis

Elevated RhoA signalling resulted in an increase of immobile E-cad and inhibited clathrin-mediated endocytosis; however, immobile E-cad was also increased when RhoA signalling was downregulated in *p120ctn* mutants. Therefore, we sought to identify the molecules responsible for this E-cad immobilisation in *p120ctn* mutants. We examined whether the GTPase Arf1, which has been reported to interact with E-cad (Shao et al., 2010; Toret et al., 2014), acts downstream of p120ctn using a GFP-tagged variant of Arf1 (*UAS::Arf1-GFP*, Lee and Harris, 2013). *UAS::Arf1-GFP* has a reduced affinity for ArfGAPs and ArfGEFs, and a reduced nucleotide exchange rate (Jian et al., 2010), which allowed us to study Arf1 without hyperactivating the pathway.

UAS::Arf1-GFP localised to both the Golgi apparatus and plasma membrane (Fig. 5A; Fig. S3A), consistent with previous reports (Lee and Harris, 2013; Shao et al., 2010). The Golgi-resident Arf1 appeared in large puncta throughout the cytoplasm (Fig. 5A; Fig. S3A). The localisation of Arf1-GFP at the plasma membrane was most apparent at the centre of the AJs (Fig. S3D). In the control, this Arf1-GFP localisation to the plasma membrane was symmetrical between the AP and DV borders ($P=0.36$; Fig. 5B). The loss of p120ctn resulted in a uniform decrease in the amount of Arf1-GFP at both borders ($P<0.0001$ and $P<0.0001$; Fig. 5B), suggesting that p120ctn promotes Arf1 localisation.

Considering the known function of Arf1 in trafficking, we tested whether the reduction in Arf1 activity was responsible for the increase in immobile CLC-GFP in the *p120ctn* mutants. We expressed a constitutively active Arf1 (*Arf1^{CA}*) in *p120ctn* mutant embryos and measured the FRAP of CLC-GFP (Fig. 5E–G). In this case, the mobile fraction of CLC-GFP was no longer different from the wild-type control ($P=0.19$; Fig. 5G; Table S1), demonstrating that the expression of *Arf1^{CA}* rescues clathrin dynamics in the *p120ctn* mutant. This is consistent with Arf1 acting downstream of p120ctn, providing a link between the p120ctn–E-cad complex and the clathrin-mediated endocytic machinery. Furthermore, we measured the dynamics of Arf1-GFP itself using FRAP (Fig. 5H,I); Arf1-GFP at the plasma membrane recovered almost completely within 25 s (Fig. 5I), which indicated a highly dynamic exchange, consistent with the known activation kinetics (Rouhana et al., 2013).

Curiously, the overexpression of p120ctn also reduced Arf1-GFP at the AP borders ($P=0.02$; Fig. 5C,D). Although the reduction of Arf1 at the DV borders was not significant ($P=0.37$), its distribution remained uniform ($P=0.18$). Because GTPases often regulate each other (Baschieri and Farhan, 2012; Singh et al., 2017), we asked whether this reduction was a consequence of p120ctn elevating RhoA signalling. We measured the membrane levels of Arf1-GFP in cells expressing RNAi against RhoGEF2 (*RhoGEF2-RNAi*; Fig. 6A), which reduces Rok amounts specifically at the AP borders (Bulgakova et al., 2013). The downregulation of RhoGEF2 resulted in an increase in the amount of Arf1-GFP at both the AP and DV borders ($P=0.022$ and $P=0.049$, respectively; Fig. 6B), demonstrating that RhoA signalling negatively regulated Arf1 localisation to the plasma membrane.

To further test whether the reduction in Arf1-GFP following the overexpression of p120ctn was due to elevated RhoA signalling, we simultaneously expressed *UAS::p120ctn* with *RhoGEF2-RNAi* (Fig. 6C,D). Indeed, we found an increase in Arf1-GFP at the plasma membrane at both borders in this case (AP, $P=0.0014$; DV, $P=0.0031$; Fig. 6D). To complement these experiments we hyperactivated RhoA signalling using *RhoA^{CA}*. We detected a

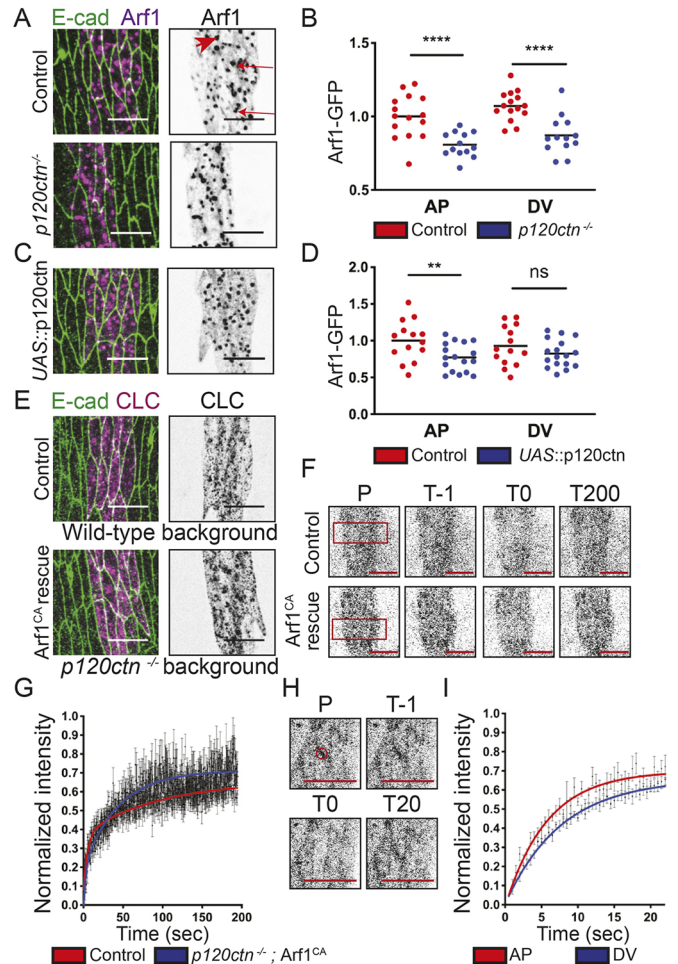


Fig. 5. Arf1 is downstream of p120ctn and promotes clathrin mediated endocytosis. (A) Apical views of epidermis expressing *UAS::Arf1-GFP* (Arf1, magenta, left; grey, right). Cell outlines are visualised using anti-E-cad antibody (green, left). The large *UAS::Arf1-GFP* puncta in the cytoplasm (large arrow) mark the Golgi. Arf1-GFP at the plasma membrane is indicated (small arrows). (B) Levels of *UAS::Arf1-GFP* in control and *p120ctn^{-/-}* mutant cells. (C) Apical views of cells co-expressing *UAS::Arf1-GFP* with *UAS::p120ctn*. (D) Levels of *UAS::Arf1-GFP* in control and p120ctn overexpressing embryos. (E) Localisation of *UAS::CLC-GFP* (grey, right; magenta, left) in control cells expressing *UAS::CLC-GFP* alone (top), and cells expressing a constitutively active Arf1 (*Arf1^{CA}*) in *p120ctn^{-/-}* mutants (bottom). Cell borders are visualised using an anti-E-cad antibody (green, left). (F,G) Representative examples (F) and quantification (G) of FRAP of *UAS::CLC-GFP* in the *Arf1^{CA}; p120ctn^{-/-}* embryos. (H,I) Representative examples (H) and quantification (I) of Arf1-GFP FRAP in control cells at both cell borders. Panels F and H show the region bleached (position P, red box) at the pre-bleach (time T-1), bleach (time T0) and the end (time T200 or T20) timepoints. Time is in seconds. Average recovery curves (mean±s.e.m.) and the best-fit curves (solid lines) are shown in G and I. Statistical analysis was done using two-way ANOVA. ns, not significant; ** $P<0.01$; **** $P<0.0001$. All best-fit and membrane intensity data are in Table S1. Each dot represents an individual embryo with means indicated by horizontal lines. $n=10-20$ embryos per genotype with a minimum of 22 cells imaged per embryo. For FRAP, 8–10 embryos were used, with a single rectangular band encompassing an *engrailed* stripe per embryo for *UAS::CLC-GFP*, and two AP and DV cell borders measured and averaged per embryo for Arf1-GFP. Scale bars: 10 μ m (A,C,E,F); 5 μ m (H).

reduction of Arf1-GFP localisation at the DV but not the AP cell border (AP, $P=0.86$; DV, $P=0.025$; Fig. 6E,F), providing further evidence for the negative action of RhoA signalling on the recruitment of Arf1-GFP to the plasma membrane. It was surprising that *RhoGEF2-RNAi* led to a uniform elevation of

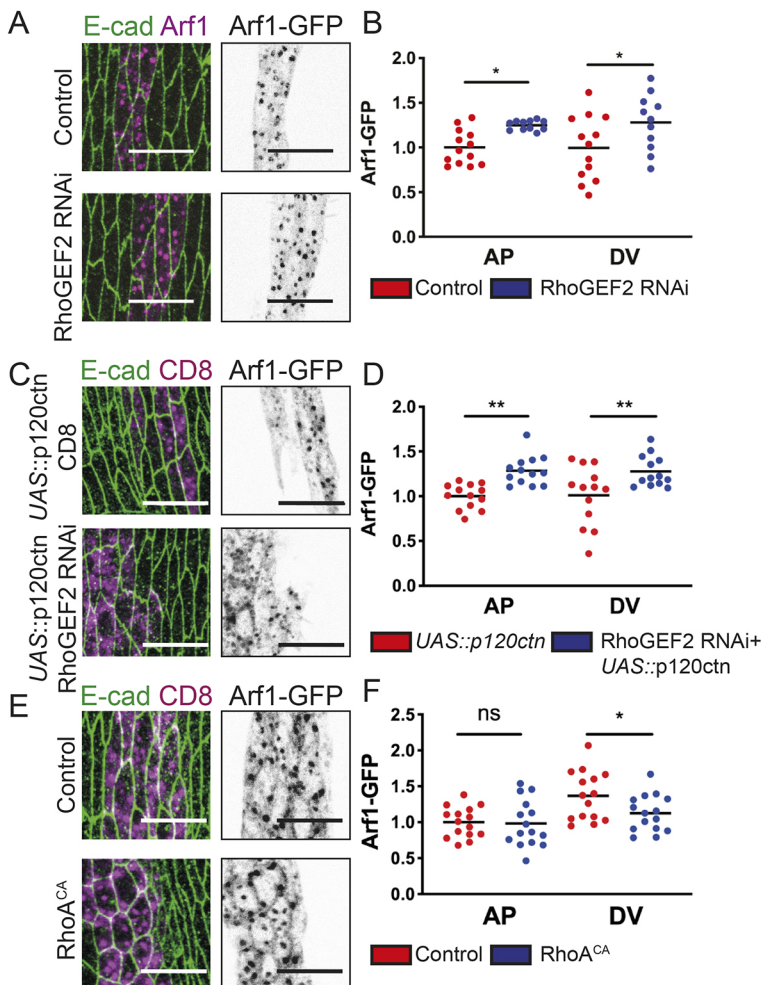


Fig. 6. Arf1 recruitment to the cell surface is inhibited by RhoA activity. (A,B) Apical view (A) and quantification (B) of UAS::Arf1-GFP in control cells (top) and cells expressing RhoGEF2 RNAi (bottom). (C,D) Apical view (C) and quantification (D) of UAS::Arf1-GFP in control cells expressing UAS::p120ctn with CD8-cherry (top) and cells co-expressing UAS::p120ctn with RhoGEF2 RNAi (bottom). (E,F) Apical view (E) and quantification (F) of UAS::Arf1-GFP in control cells and cells expressing RhoA^{CA}. Expressing cells are visualised using UAS::Arf1-GFP (grey, right; magenta, left) and cell outlines visualised using an antibody against E-cad (green, left) in A, C and E. Statistical analysis was performed using two-way ANOVA. ns, not significant; * $P<0.05$; ** $P<0.01$. All best-fit and membrane intensity data are in Table S1. Each dot represents an individual embryo, with means indicated by horizontal lines. $n=10$ –20 embryos per genotype with a minimum of 26 cells imaged per embryo. Scale bars: 10 μ m.

Arf1-GFP, because it affects Rok only at the AP borders (Bulgakova et al., 2013). Indeed, Arf1 was uniformly localised at the plasma membrane in all cases. We inferred that the effect of RhoGEF2-RNAi on Arf1 at the DV borders was indirect – reduced RhoA signalling results in elevated recruitment of Arf1 at the AP borders, followed by rapid redistribution around the cell periphery and an overall elevation of Arf1-GFP at the cell surface.

Finally, to ask whether Arf1 has any action on RhoA and actomyosin, we measured the membrane localisation of MyoII-YFP upon the upregulation of Arf1 signalling using Arf1^{CA} (Fig. S3B). MyoII-YFP localisation was indistinguishable between control and Arf1^{CA}-expressing cells (Fig. S3C), suggesting that RhoA signalling in the embryonic epidermis is independent of Arf1. Overall, we conclude that Arf1 was reduced at the plasma membrane in p120ctn overexpressing cells due to the elevation of RhoA signalling. The reduction of Arf1 upon loss of p120ctn appeared independent of RhoA, and we suggest that it is caused by reduction of Arf1 recruitment and/or activation by p120ctn.

Adhesion dynamics regulate cell shape

So far, we demonstrated that p120ctn regulates actomyosin via RhoA signalling, and E-cad dynamics via both RhoA and Arf1. Next, we asked how this regulatory network contributes to the cell shape changes caused by altered p120ctn levels. We first examined how the inhibition and hyperactivation of Arf1 alone affected cell shape using a dominant-negative Arf1 (Arf1^{DN}; Fig. 7A). Prolonged exposure to Arf1^{DN} resulted in small rounded cells (Fig. S3E) and no surviving

larvae, consistent with previous reports (Carvajal-Gonzalez et al., 2015), likely due to gross perturbation of post-Golgi protein transport causing cell death (Jian et al., 2010; Luchsinger et al., 2018). Therefore, we acutely induced the expression of Arf1^{DN} using a temperature sensitive GAL80^{ts}. The cells that expressed the Arf1^{DN} had a reduced aspect ratio ($P=0.003$; Fig. 7A,B). This suggests that the reduction of endocytosis, and therefore increased immobile E-cad, is sufficient to reduce the cell aspect ratio. This conclusion is also supported by the reduced aspect ratio observed in other phenotypes in which the immobile fraction of E-cad was increased: namely the overexpression of p120ctn and the expression of RhoA^{CA} ($P<0.0001$; Fig. 7C,D). To test whether an increase in E-cad immobility alone is sufficient to reduce cell elongation, we used an alternative approach to inhibit E-cad endocytosis by overexpressing a dominant-negative form of the dynamin Shibire (Shi^{DN}; Fig. 7E). Expression of Shi^{DN} increases the immobile fraction of E-cad at the plasma membrane similarly to the loss of p120ctn (Bulgakova et al., 2013). Indeed, cells expressing Shi^{DN} had a reduced aspect ratio in comparison to control cells ($P=0.0002$; Fig. 7E,F).

Finally, to investigate whether the perturbations in Arf1 and RhoA signalling caused by changes in p120ctn levels were responsible for the defects in cell morphology, we performed genetic rescue experiments. We expressed Arf1^{CA} in p120ctn mutant embryos and found that the aspect ratio reduction was completely rescued ($P=0.57$ in comparison to control; Fig. 7G,H). To complement this, we downregulated RhoA signalling using RhoGEF2 RNAi in cells overexpressing p120ctn (Fig. 7I). The aspect ratio of these cells was

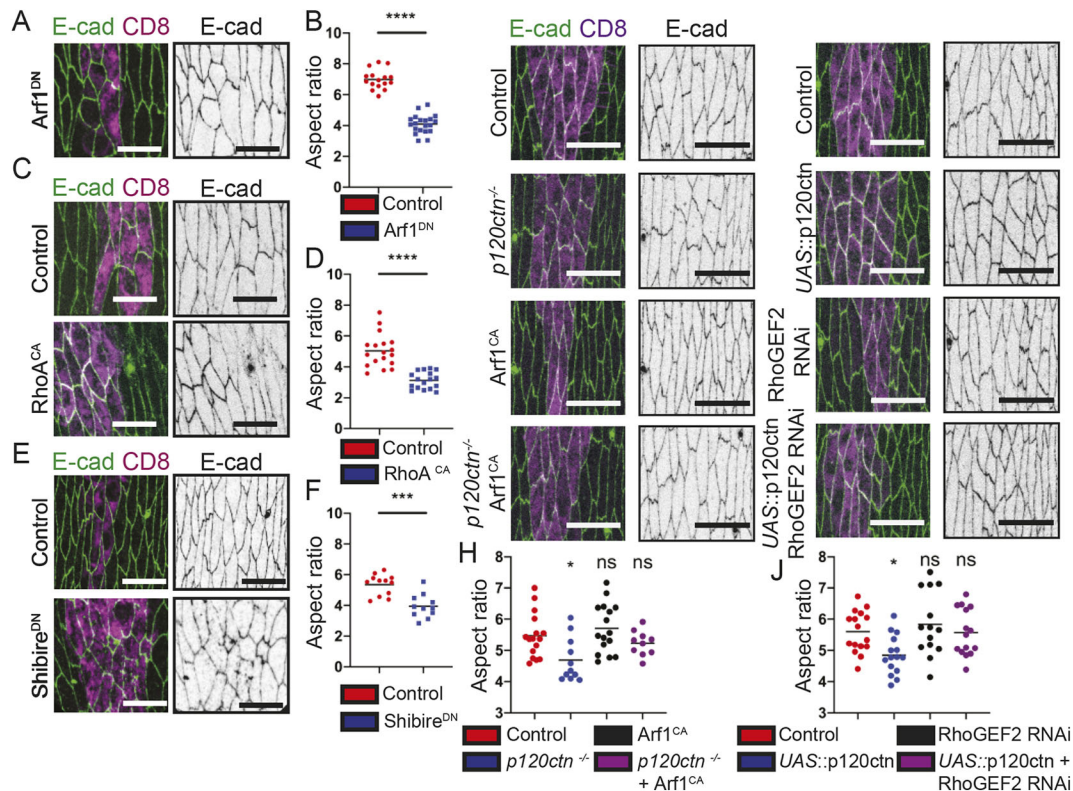


Fig. 7. Reduced cell elongation after inhibition of E-cad dynamics, and its rescue by modulating Arf1 and RhoA signalling. (A,B) Apical views (A) and cell aspect ratio (B) of epidermal cells following the downregulation of Arf1 (post induction of Arf1^{DN} expression for 4 h). (C,D) Apical views (C) and cell aspect ratio (D) following upregulation of RhoA signalling using a constitutively active construct (RhoA^{CA}). (E,F) Apical views (E) and cell aspect ratio (F) of epidermal cells following the inhibition of endocytosis using the expression of a dominant-negative variant of dynamin (Shibire^{DN}). (G,H) Apical views (G) and cell aspect ratio (H) in control cells, *p120ctn* mutant cells, either expressing Arf1^{CA} or not. (I,J) Apical views (I) and cell aspect ratio (J) in control cells, and cells expressing UAS::p120ctn alone, RhoGEF2 RNAi alone, or co-expressing UAS::p120ctn with RhoGEF2 RNAi. Cell outlines are visualised using E-cad–GFP. Statistical analysis used a two-tailed Student's *t*-test with Welch's correction, except for the rescue experiments where a one-way ANOVA with Dunnett's post-hoc test was used. ns, not significant; **P*<0.05; ****P*<0.001; *****P*<0.0001. All best-fit and membrane intensity data are in Table S1. Each dot represents an individual embryo, with means indicated by horizontal lines. *n*=10–20 embryos per genotype with a minimum of 17 cells imaged per embryo. Scale bars: 10 μ m.

again indistinguishable from the control (*P*=0.99; Fig. 7J). Therefore, the defects in cell elongation caused by the loss or elevation of p120ctn are rescued by compensating for the Arf1 and RhoA signalling pathways, respectively.

Overall, these results indicate that the dynamics of intercellular adhesion, mediated via endocytosis of E-cad, is an important factor in determining the elongation of epidermal cells.

DISCUSSION

Epithelial cells *in vitro* are usually isotropic, and the application of external stretching or compressing forces induces an initial anisotropy in their shape (elongation), which is quickly resolved through cell rearrangements and divisions, or tissue three-dimensional deformation (Duda et al., 2019; Latorre et al., 2018; Nestor-Bergmann et al., 2019). By contrast, there are multiple examples of highly anisotropic elongated cells in whole organisms, including mammalian skin and the epidermal cells used in this study (Fig. 8A; Aw et al., 2016; Box et al., 2019). These elongated shapes are necessary for correct tissue and organism morphogenesis (Box et al., 2019; McCleery et al., 2019).

In this study, we focused on the regulation of such elongated cell shape through the crosstalk between E-cad-mediated adhesion and cortical actomyosin. We provide *in vivo* evidence that p120ctn, a known regulator of E-cad dynamics and endocytosis (Bulgakova and Brown, 2016; Ireton et al., 2002; Nanes et al., 2012; Sato et al., 2011),

mediates this crosstalk and regulates cell shape. It does so by promoting the activities of at least two small GTPases with opposing effects on E-cad dynamics: RhoA, which inhibits E-cad turnover; and Arf1, which promotes it (Fig. 8B). We show an interplay between these GTPases, with RhoA preventing the localisation of Arf1 to plasma membrane (Fig. 8B). As a result, both the depletion and overexpression of p120ctn lead to an increase in immobile E-cad at the cell surface: depletion is likely to do so through directly limiting Arf1 recruitment to the plasma membrane, whereas overexpression does so through elevating RhoA activity, which then inhibits Arf1. Finally, although p120ctn normally colocalises with E-cad and is at higher levels on the DV borders, we show that it regulates RhoA activity only at the AP borders, suggesting a tension-dependent function for p120ctn.

We demonstrate that the elongated cell shape is accompanied by anisotropic forces in the epidermis: while the AP borders are under tension, the DV borders are under compression. Most previous laser ablation experiments have reported positive velocities of the initial recoil when the vertices of the manipulated junction move apart (Sugimura et al., 2016). The only exception apart from our work, to our knowledge, is the case of anisotropic tissue stress in the amnioserosa, where a similar negative recoil was observed during germ-band retraction (McCleery et al., 2019). This germ-band retraction drives the elongation of epidermal cells (Gomez et al., 2016; McCleery et al., 2019). We suggest that the anisotropic pushing

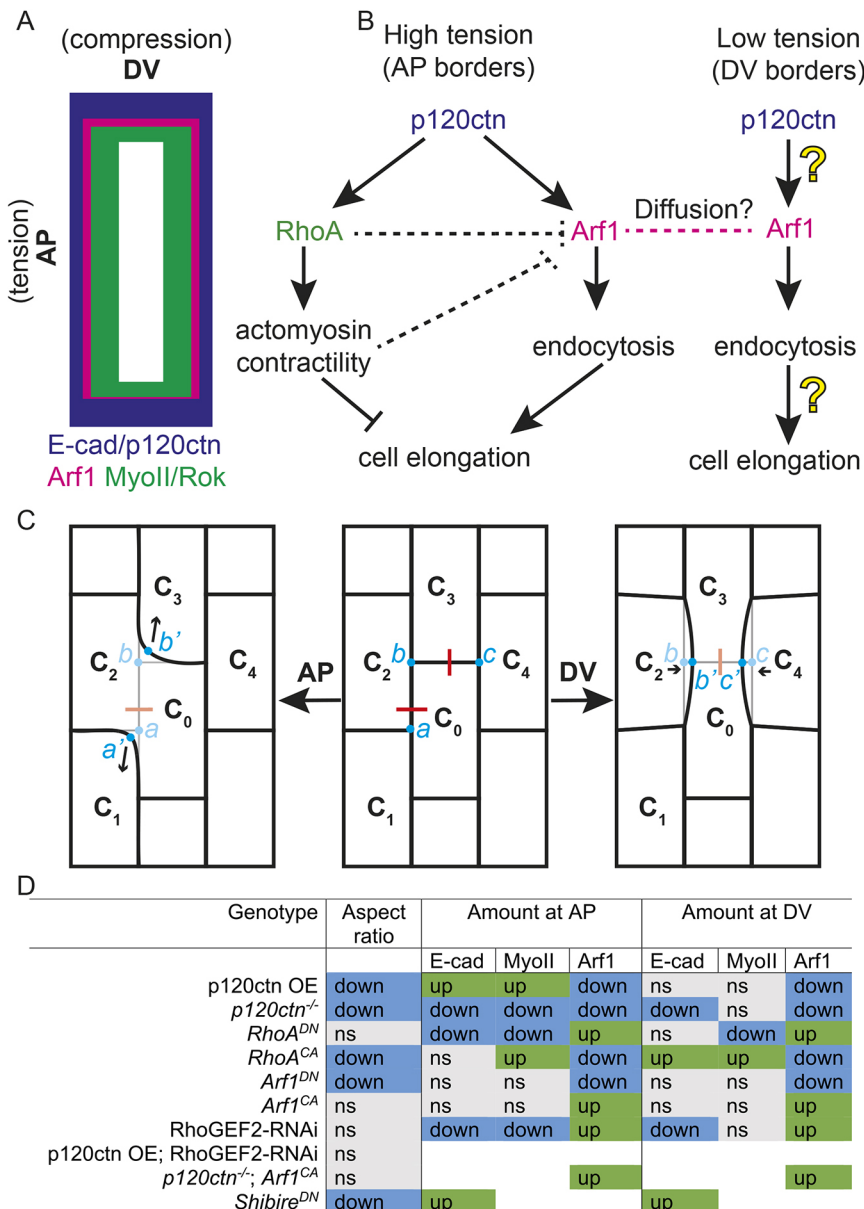


Fig. 8. Models of cell shape regulation, laser ablation experiments and a summary of phenotypes.

(A) Schematic of cellular anisotropy in the embryonic epidermis of stage 15 *Drosophila* embryos. E-cad and p120ctn (blue) are enriched at the DV borders, whereas MyoII and Rok (green) are enriched at the AP borders, and Arf1 (magenta) is uniform. The long AP borders are under tension, whereas the short DV borders are under compressive force. (B) Model of cell shape regulation by actomyosin and E-cad dynamics. AP borders: high cortical tension and actomyosin contractility inhibit cell elongation, whereas adhesion dynamics promotes elongation. Actomyosin is activated downstream of RhoA signalling, whereas Arf1 GTPase promotes clathrin-mediated endocytosis. RhoA additionally inhibits this endocytosis by either directly or indirectly preventing Arf1 localisation (dashed lines). Finally, both RhoA and Arf1 are activated downstream of p120ctn at the long AP borders. DV borders: tension and RhoA activity are low and are not regulated by p120ctn. Arf1 promotes E-cad endocytosis at the DV borders. Arf1 is highly diffusive and its levels at the DV borders are likely to be influenced by recruitment at the AP borders via diffusion (magenta dashed line). It is unclear whether Arf1 or other molecules are regulated by p120ctn, or if E-cad dynamics contributes to cell shape at this border (question marks). (C) Schematic interpretation of laser ablation in the embryonic epidermis. Middle: before ablation, with the cells and vertices involved indicated. Left: ablation of an AP cell border. Surface minimisation by cells C₁ and C₃ shifts the position of the released vertices a and b to new positions a' and b' (arrows), increasing the distance. Right: ablation of a DV cell border. Expansion of cells C₂ and C₄ to minimise their surfaces reduces the distance between vertices b and c to new positions b' and c'. (D) Summary of the cell shape phenotypes and protein distributions in the genotypes presented in the study. ns, no significant change.

by the amnioserosa is likely to be the source of the observed compression, as also suggested previously (Hirano et al., 2009).

In the case of an isotropic tissue, the behaviour of cells can be represented as those of soap bubbles (Hayashi and Carthew, 2004), which tend to minimise their surfaces. This leads to a shift of vertices after ablation to new positions such that the distance between them increases. Such a situation is usually modelled as a Kelvin–Voigt fibre (Fernandez-Gonzalez et al., 2009). In the case of anisotropic cells, which are strongly elongated, the situation can be different depending on which type of border is ablated (Fig. 8C). In the case of AP borders, the distance between the vertices increases as cells obtain freedom to minimise their surfaces (Fig. 8C). However, in the case of DV borders, the released stress enables cells anterior and posterior to the border to expand due to the same surface minimisation mechanism, decreasing the distance between vertices, as observed in the experiments (Fig. 8C). It can be concluded that the Kelvin–Voigt fibre model is not directly applicable to such anisotropic cells. We speculate that this is a strongly dynamic process: swift reduction of the distance results in over-compression, leading to expansion. We

suggest that this process is governed by surface tension of cell membranes and should resemble oscillations of soap bubbles (Saye, 2017). It is still unclear whether, after expansion, a new compression stage can start.

We have shown that the increase of immobile E-cad, and thus the inhibition of junctional remodelling, following expression of Arf1^{DN}, Shi^{DN}, RhoA^{CA}, and loss of p120ctn (Fig. 8D), prevents the elongation of cells in the *Drosophila* embryonic epidermis (Fig. 8B), suggesting a central role for E-cad dynamics in cell elongation. The contractility of actomyosin normally acts to reduce the surface length, whereas the levels of adhesion acts oppositely (Lecuit and Lenne, 2007). Indeed, the strongest reduction in cell elongation was observed upon expression of RhoA^{CA}, which increased the immobile fraction of E-cad and activated actomyosin contractility. At the same time, an increase in immobile E-cad seems sufficient to reduce the junctional length, as observed both in p120ctn mutant cells and those expressing Arf1^{DN}. Therefore, we propose that cell elongation is the product of the counteraction of E-cad dynamics and cortical contractility.

Although the roles of RhoA and p120ctn in E-cad endocytosis are long-established (Davis et al., 2003; Ellis and Mellor, 2000), the Arf1-dependent recruitment of clathrin has only been shown to occur at the Golgi by recruiting the Adaptor 1 protein (Carvajal-Gonzalez et al., 2015). The function of Arf1 at the plasma membrane has been described in dynamin-independent endocytosis, which was presumed to be clathrin-independent (Kumari and Mayor, 2008). We have shown that the capacity of Arf1 to recruit clathrin is exploited by p120ctn to facilitate the endocytosis of E-cad. Whether this requires AP2, a plasma membrane clathrin adaptor, has yet to be determined. This finding provides a mechanistic insight into the pro-endocytic activity of p120ctn (Bulgakova and Brown, 2016; Sato et al., 2011) and elaborates the number of known p120ctn interactors. The activities of Arf1 and RhoA are antagonistic, which was also seen during the cellularisation of the early embryo (Lee and Harris, 2013).

In contrast to Arf1, the regulation of RhoA by p120ctn has been shown in many studies, although the exact effects and mechanisms seem to be context-dependent (Anastasiadis et al., 2000; Derksen and van de Ven, 2017; Lang et al., 2014; Taulet et al., 2009; Yu et al., 2016; Zebda et al., 2013). We demonstrate that in the epidermal cells of *Drosophila* embryos, p120ctn leads to activation of RhoA at the AP but not DV borders (Fig. 8B). In contrast, we show that p120ctn loss uniformly reduces recruitment of Arf1 to the plasma membrane. However, we also find that Arf1 is very dynamic and the changes at the DV borders, for example upon the downregulation of RhoGEF2, are likely to be an indirect consequence of the effect at the AP borders (Fig. 8B). It is therefore currently unclear whether p120ctn performs any direct activity at the DV borders, or promotes RhoA and Arf1 signalling only at the high-tension AP borders. Indeed, recent evidence suggests that p120ctn has mechanosensing properties (Iyer et al., 2019). Using laser ablation we demonstrated that p120ctn modulates tension at these AP borders, providing evidence for the role of p120ctn in mechanotransduction. It is yet to be determined whether p120ctn is directly sensing the tension through a conformational change similarly to other components of cell–cell adhesion such as α -catenin and vinculin (Bays and DeMali, 2017; Yao et al., 2014), or is regulated by another mechanotransducer.

Taken together, our findings demonstrate that cell elongation in a tissue is regulated through the opposing action of actomyosin contractility and adhesion endocytosis, which are, however, closely interconnected and regulate each other. Adhesion components modify actomyosin, while the latter alters adhesion endocytosis. Considering that all of the molecules studied are expressed in all epithelia across evolution, we speculate that this system is likely to be more broadly applicable in development and a general feature of cell biology.

MATERIALS AND METHODS

Fly stocks and genetics

Flies were raised on standard medium. The GAL4/UAS system (Brand and Perrimon, 1993) was used for all the specific spatial and temporal expression of transgenic and RNAi experiments. The GAL4 expression driver used for all experiments was *engrailed::GAL4* (*en::GAL4*, Bloomington number 30564). The following fly stocks were used in this study (Bloomington number included where applicable): E-cad-GFP (*shg::E-cad-GFP*, 60584), E-cad-Cherry (*shg::E-cad-Cherry*, 59014), *UAS::CD8-Cherry* (27392), *UAS::CLC-GFP* (7109), *UAS::Arf1-GFP* (gift from Tony Harris, University of Toronto, Canada), Zipper-YFP (MyoII-YFP, Kyoto Stock Center 115082), *sqh::Rok^{K116A}-Venus* (gift from Jennifer Zallen, Sloan Kettering Cancer Center, New York City, USA), *UAS::Arf1-T31N* (DN) and *UAS::Arf1-Q71 L* (CA) (Dottermusch-Heidel et al., 2012), *UAS::Rho1-N19* (DN) (7328), *UAS::Rho1-V14* (CA) (7330), *UAS::RhoGEF2-RNAi* (VDRC 110577), *ubi::AniRBD-GFP* (RBD-GFP, Munjal et al., 2015), *tubulin::*

GAL80^{TS} (7017), *ubi::p120ctn-GFP* (7190), *UAS::p120ctn-GFP* (7192), *UAS::Shibire^{K44A}* (*Shi^{DN}*, 5822), and *UAS::LifeAct-GFP* (57326). The *p120ctn* mutant embryos (*p120ctn³⁰⁸/Δp120*) were derived from crossing two stocks: homozygously viable *p120ctn³⁰⁸* females (Myster et al., 2003) with homozygously lethal *Df(2R)M41A8/CyO*, *twi::Gal4*, *UAS::GFP* males (740). Thus, the *p120ctn* mutants examined lacked both maternal and zygotic contributions. In all experiments when necessary, additional copies of *UAS::CD8-Cherry* were used to balance the Gal4:UAS ratio across genotypes in each dataset.

Embryo collection and fixation

Embryos were collected at 25°C at 3-h time intervals and allowed to develop at 18°C for 21 h to reach the desired developmental stage, except for the acute induction experiments, where embryos were allowed to develop for 13 h at 18°C and shifted to 29°C for 4 h. Then embryos were dechorionated using 50% sodium hypochlorite (Invitrogen) in water for 4 min and extensively washed with deionised water prior to fixation. Fixation was performed with a 1:1 solution of 4% formaldehyde (Sigma) in PBS (phosphate buffered saline) and heptane (Sigma) for 20 min on an orbital shaker at room temperature. Embryos were then devitellinised in 1:1 solution of methanol and heptane for 20 s with vigorous agitation. Following subsequent methanol washes, the fixed embryo specimens were stored at −20°C in methanol until required.

Embryo live imaging

Embryos were collected and dechorionated as described above. Once washed with deionised water embryos were transferred to apple-juice agar segments upon microscope slides. Correct genotypes were selected under a fluorescence microscope (Leica) using a needle. Embryos were positioned and orientated in a row consisting of 6–10 embryos per genotype. Following this, embryos were transferred to prepared microscope slides with Scotch tape and coverslip bridge and embedded in Halocarbon oil 27 (Sigma). Embryos were left to aerate for 10 min prior to covering with a coverslip and imaging.

For laser ablation, following orientation and positioning the embryos were transferred to a 60 mm×22 mm coverslip which had been prepared by applying 10 μ l of heptane glue along a strip in the middle of the coverslip orientated with the long axis. The coverslip was attached to a metal slide cassette (Zeiss), and the embryos were embedded in Halocarbon oil 27 before imaging.

Molecular cloning

The p120ctn full-length cDNA was obtained from Berkeley Drosophila Genome Project (BDGP), supplied in a pBSSK vector. This was subcloned into plasmid pUAS-k10.attB (DGRC) using standard restriction digestion with NotI and BamHI (New England Biolabs) followed by ligation with T4 DNA ligase (New England Biolabs) and transformation into DH5 α competent *E. coli* cells (Thermo Fisher Scientific). Prior to injection, plasmids were test digested and sequenced (Core Genomic Facility, University of Sheffield). Plasmids were prepared for injection using standard miniprep extraction (Qiagen) and submitted for injection (Microinjection service, Department of Genetics, University of Cambridge) into the attP-86Fb stock (Bloomington stock 24749). Successful incorporation of the transgene was determined by screening for (*w*⁺) in the F1 progeny.

Immunostaining

The embryos were washed three times in 1 ml of PBST (PBS with 0.05% Triton) with gentle rocking. Blocking of the embryos prior to staining was done in 300 μ l of a 1% NGS (normal goat serum; New England Biolabs) in PBST for 1 h at room temperature with gentle rocking. For staining, the blocking solution was removed, 300 μ l of the primary antibody [1:100 rat anti-E-cad (DCAD2, DSHB), 1:10 mouse anti-engrailed (4D9, DSHB), or 1:500 anti-Golgi (Golgin-245, Calbiochem)] in fresh blocking solution was added and the embryos were incubated overnight at 4°C with orbital rotation. Then, embryos were washed three times with 1 ml of PBST. A 300 μ l 1:300 dilution of the secondary antibody (goat Cy3- or Cy5-conjugated IgG, Invitrogen) was added, and the embryos incubated either overnight at 4°C with orbital rotation or for 2 h at room temperature. Then

embryos were washed three times with PBST, following which they were incubated with 50–70 μ l of Vectashield (Vector Laboratories) and allowed to equilibrate for a period of 2 h before being mounted on microscope slides (Thermo).

Microscopy, data acquisition and FRAP

All experiments except for laser ablation were performed using an upright Olympus FV1000 confocal microscope with a 60 \times /1.40 NA oil immersion objective. Shi^{DN}-expressing embryos and the corresponding control were imaged using 100 \times /1.40 NA UPlanApo objective. All measurements were made on dorsolateral epidermal cells of embryos, which were near or just after completion of dorsal closure, corresponding to the end of stage 15 of embryogenesis. For fixed samples, 16-bit images were taken at a magnification of 0.051 μ m/pixel (1024 \times 1024 pixel *xy*-image) or 0.062 μ m/pixel (Shi^{DN} embryos and the corresponding control) with a pixel dwell of 4 μ m/pixel. For each embryo, a *z*-axis sectional stack through the plane of the AJs was taken, which consisted of six sections with a 0.38 μ m intersectional spacing. The images were saved in the Olympus binary image format for further processing.

For E-cad FRAP (adapted from Bulgakova et al., 2013) 16-bit images were taken at a magnification of 0.093 μ m/pixel (320 \times 320 pixel *xy*-image). In each embryo, several circular regions of 1 μ m radius were photobleached at either DV or AP junctions resulting in one bleach event per cell. Photobleaching was performed with eight scans at 2 μ s/pixel at 50–70% 488 nm laser power, resulting in the reduction of E-cad–GFP signal by 60–80%. A stack of six *z*-sections spaced by 0.38 μ m was imaged just before photobleaching and immediately after photobleaching, and then subsequently at 20 s intervals for a total of 15 min.

Because the rate of endocytosis depends on external factors, such as temperature, controls were examined in parallel with experimental conditions in all experiments with CLC–GFP. For CLC–GFP FRAP, 16-bit images were taken at a magnification of 0.051 μ m/pixel (256 \times 256 pixel *xy*-image). In each embryo a single plane was selected in the centre of the AJ band using E-cad–Cherry fluorescence for positioning. An area encompassing a transverse region orthogonal to the axis of the *engrailed*-expressing cells was selected (140 \times 60 pixels) and photobleached with a single scan at 2 μ m/pixel using 100% 488 nm laser power, resulting in reduction of CLC–GFP signal by 70–80%. Images were taken using continuous acquisition at a frame rate of 2 s^{−1}. Prior to bleaching, a sequence of ten images was taken, and a total of 400 frames, corresponding to 3.5 min, were taken.

Data processing and statistical analysis

Membrane intensity and cell shape

Images were processed in Fiji (<https://fiji.sc>) by generating average intensity projections of the channel required for quantification. Masks were created by processing background-subtracted maximum intensity projections using the Tissue Analyzer plugin in Fiji (Aigouy et al., 2016). Quantification of the membrane intensity at the AP and DV borders and cell elongation (aspect ratio) was done as described previously (Bulgakova and Brown, 2016), using a custom-built Matlab script that can be found at <https://github.com/nbul/Intensity>. In short, cells were identified as individual objects using the created masks, and their eccentricities were calculated. The aspect ratio was calculated from the eccentricity as: $AR = 1/\sqrt{1 - e^2}$, where e is eccentricity. At the same time, the individual borders were identified as objects by subtracting a dilated mask of vertices from a dilated mask of cell outlines. The mean intensity and orientation of each border were calculated. The average border intensities (0–10° for the AP and 40–90° for the DV borders, relative to cell mean orientation) were calculated for each embryo and used as individual data points to compare datasets. The average cytoplasmic intensity was used for the background subtraction. In the case of quantification of Arf1–GFP membrane intensity, due to high Arf1–GFP presence inside cells both in the Golgi and cytoplasm, the mean intensity of embryonic areas not expressing the GFP-tagged transgene were used for background subtraction. Statistical analysis was performed in Graphpad Prism (<https://www.graphpad.com/scientific-software/prism/>). First, the data was cleaned using ROUT detection of outliers in Prism followed by testing for normal distribution (D'Agostino–Pearson normality test). Then,

the significance for parametric data was tested by either a two-way ANOVA or two-tailed *t*-test with Welch's correction.

Total protein

A dilated mask, outlining the cell perimeter and encompassing the plasma membrane signal, was used to measure the cumulative intensity of pixels.

E-cad FRAP

Images were processed by using the grouped *z*-projector plugin in Fiji to generate average intensity projections for each timepoint. Following this, the bleached region of interest (ROI), control ROI and background intensity were manually measured for each timepoint. This data was processed in Microsoft Excel. First, the intensity of the bleached ROI at each time point was background subtracted and normalised as follows: $I_n = (F_n - BG_n) / (FC_n - BG_n)$, where F_n is the intensity of the bleached ROI at the timepoint n , FC_n is the intensity of the control unbleached ROI of the same size at the plasma membrane at the timepoint n , and BG_n is the background intensity, measured with the same size ROI in the cytoplasm at the timepoint n . Then, the relative recovery at each time point was calculated using the following formula: $R_n = (I_n - I_1) / (I_0 - I_1)$, where I_n , I_1 and I_0 are normalised intensities of the bleached ROI at time point n , immediately after photobleaching and before photobleaching, respectively. These values were input into Prism and nonlinear regression analysis was performed to test for the best fit model and whether recoveries were significantly different between cell borders or genotypes. The recovery was fit to either a single exponential model in the form of $f(t) = 1 - F_{im} - A_1 e^{-t/T_{fast}}$, or to a bi-exponential model in the form of $f(t) = 1 - F_{im} - A_1 e^{-t/T_{fast}} - A_2 e^{-t/T_{slow}}$, where F_{im} is the size of the immobile fraction, T_{fast} and T_{slow} are the half-times, and A_1 and A_2 are amplitudes of the fast and slow components of the recovery. An F-test was used to choose the model and compare datasets.

CLC-GFP FRAP

Measurements of all intensities, i.e. the bleached ROI, control ROI and the background, and normalisation were done using a custom-built Matlab script (<http://github.com/nbul/FRAP>) using the same algorithm as described for E-cad FRAP. Curve fitting and statistical analysis was performed in Graphpad Prism using a nonlinear regression analysis as described for E-cad FRAP.

Laser ablation

Nanoablation of single junctions was performed to provide a measure of junctional tension. The *Drosophila* embryonic epidermis is uniquely suited to the study of tissue compression *in vivo*. Though tissue compression can lead to events such as bending, buckling and folding in epithelia, epithelia can accommodate large and rapid compressive forces extremely well (Wyatt et al., 2020). Additionally, the ability of the embryonic epidermis to buckle is abolished by the presence of vitelline membrane, which limits any tissue movement outside of its *z*-plane. Embryos were imaged on a Zeiss LSM 880 microscope with an Airyscan detector, an 8-bit image at 0.053 μ m/pixel (512 \times 512 pixel *xy*-Image) resolution with a 63 \times objective (1.4 NA) at 5 \times zoom and 2 \times averaging was used. An illumination wavelength of 488 nm and 0.5% laser power were used. Images were captured with a 0.5 μ m *z*-spacing. Narrow rectangular ROIs were drawn across the centre of single junctions and this region was ablated using a pulsed TiSa laser (Chameleon), tuned to 760 nm at 45% power. 0.95 μ s/pixel dwell for a single *z*-stack iteration was used for pulse duration. Embryos were imaged continuously in a *z*-stack consisting of three *z*-slices. The distance between the vertices at the ends of ablated junctions was measured throughout the time course of the experiment and was expressed as a proportional change in distance relative to pre-ablation length. Statistical analysis was performed in Graphpad Prism using a two-tailed *t*-test with Welch's correction.

Acknowledgements

The authors thank Rob Tetley and Yanlan Mao for assistance with laser ablation experiments and Nadezhda M. Bulgakova for assistance with interpreting these experiments. The authors also wish to acknowledge the advice and guidance of Professor David Strutt, University of Sheffield, and his lab. The authors thank the technical staff of the Wolfson Light Microscopy Facility (LMF) and the *Drosophila* Facility at the University of Sheffield.

Competing interests

The authors declare no competing or financial interests.

Author contributions

Conceptualization: N.A.B.; Methodology: J.G., N.A.B.; Software: N.A.B.; Validation: J.G.; Formal analysis: J.G., N.A.B.; Investigation: J.G., N.A.B.; Resources: N.A.B.; Data curation: J.G., N.A.B.; Writing - original draft: J.G., N.A.B.; Writing - review & editing: J.G., N.A.B.; Visualization: J.G., N.A.B.; Supervision: N.A.B.; Project administration: N.A.B.; Funding acquisition: N.A.B.

Funding

This work was supported by a grant from the UK Biotechnology and Biological Sciences Research Council (BB/P007503/1).

Supplementary information

Supplementary information available online at
<https://jcs.biologists.org/lookup/doi/10.1242/jcs.242321.supplemental>

Peer review history

The peer review history is available online at
<https://jcs.biologists.org/lookup/doi/10.1242/jcs.242321.reviewer-comments.pdf>

References

- Adams, C. L., Nelson, W. J. and Smith, S. J. (1996). Quantitative analysis of cadherin-catenin-actin reorganization during development of cell-cell adhesion. *J. Cell Biol.* **135**, 1899-1911. doi:10.1083/jcb.135.6.1899
- Aigouy, B., Umetsu, D. and Eaton, S. (2016). Segmentation and quantitative analysis of epithelial tissues. *Methods Mol. Biol.* **1478**, 227-239. doi:10.1007/978-1-4939-6371-3_13
- Amano, M., Nakayama, M. and Kaibuchi, K. (2010). Rho-kinase/ROCK: A key regulator of the cytoskeleton and cell polarity. *Cytoskeleton* **67**, 545-554. doi:10.1002/cm.20472
- Anastasiadis, P. Z., Moon, S. Y., Thoreson, M. A., Mariner, D. J., Crawford, H. C., Zheng, Y. and Reynolds, A. B. (2000). Inhibition of RhoA by p120 catenin. *Nat. Cell Biol.* **2**, 637-644. doi:10.1038/35023588
- Aw, W. Y., Heck, B. W., Joyce, B. and Devenport, D. (2016). Transient tissue-scale deformation coordinates alignment of planar cell polarity junctions in the mammalian skin. *Curr. Biol.* **26**, 2090-2100. doi:10.1016/j.cub.2016.06.030
- Baschieri, F. and Farhan, H. (2012). Crosstalk of small GTPases at the golgi apparatus. *Small GTPases* **3**, 80-90. doi:10.4161/sgtp.19842
- Bays, J. L. and DeMali, K. A. (2017). Vinculin in cell-cell and cell-matrix adhesions. *Cell. Mol. Life Sci.* **74**, 2999-3009. doi:10.1007/s00018-017-2511-3
- Blankenship, J. T., Backovic, S. T., Sanny, J. S. P., Weitz, O. and Zallen, J. A. (2006). Multicellular rosette formation links planar cell polarity to tissue morphogenesis. *Dev. Cell* **11**, 459-470. doi:10.1016/j.devcel.2006.09.007
- Box, K., Joyce, B. W. and Devenport, D. (2019). Epithelial geometry regulates spindle orientation and progenitor fate during formation of the mammalian epidermis. *eLife* **8**.
- Braga, V. M. M., Machesky, L. M., Hall, A. and Hotchin, N. A. (1997). The small GTPases rho and rac are required for the establishment of cadherin-dependent cell-cell contacts. *J. Cell Biol.* **137**, 1421-1431. doi:10.1083/jcb.137.6.1421
- Brand, A. H. and Perrimon, N. (1993). Targeted gene expression as a means of altering cell fates and generating dominant phenotypes. *Development* **118**, 401-415.
- Bulgakova, N. A. and Brown, N. H. (2016). Drosophila p120-catenin is crucial for endocytosis of the dynamic E-cadherin-Bazooka complex. *J. Cell Sci.* **129**, 477-482. doi:10.1242/jcs.177527
- Bulgakova, N. A., Grigoriev, I., Yap, A. S., Akhmanova, A. and Brown, N. H. (2013). Dynamic microtubules produce an asymmetric E-cadherin-Bazooka complex to maintain segment boundaries. *J. Cell Biol.* **201**, 887-901. doi:10.1083/jcb.201211159
- Carnahan, R. H., Rokas, A., Gaucher, E. A. and Reynolds, A. B. (2010). The molecular evolution of the p120-catenin subfamily and its functional associations. *PLoS ONE* **5**. doi:10.1371/journal.pone.0015747
- Carvajal-Gonzalez, J. M., Balmer, S., Mendoza, M., Dussert, A., Collu, G., Roman, A. C., Weber, U., Ciruna, B. and Mlodzik, M. (2015). The clathrin adaptor AP-1 complex and Arf1 regulate planar cell polarity in vivo. *Nat. Commun.* **6**.
- Chalut, K. J. and Paluch, E. K. (2016). The actin cortex: a bridge between cell shape and function. *Dev. Cell* **38**, 571-573. doi:10.1016/j.devcel.2016.09.011
- Chang, H. C., Newmyer, S. L., Hull, M. J., Ebersold, M., Schmid, S. L. and Mellman, I. (2002). Hsc70 is required for endocytosis and clathrin function in *Drosophila*. *J. Cell Biol.* **159**, 477-487. doi:10.1083/jcb.200205086
- Chugh, P. and Paluch, E. K. (2018). The actin cortex at a glance. *J. Cell Sci.* **131**.
- Chugh, P., Clark, A. G., Smith, M. B., Cassani, D. A. D., Dierkes, K., Ragab, A., Roux, P. P., Charras, G., Salbreux, G. and Paluch, E. K. (2017). Actin cortex architecture regulates cell surface tension. *Nat. Cell Biol.* **19**, 689-697. doi:10.1038/ncb3525
- Clark, A. G., Wartlick, O., Salbreux, G. and Paluch, E. K. (2014). Stresses at the cell surface during animal cell morphogenesis. *Curr. Biol.* **24**, R484-R494. doi:10.1016/j.cub.2014.03.059
- Daniel, J. M. and Reynolds, A. B. (1995). The tyrosine kinase substrate P120(Cas) binds directly to E-cadherin but not to the adenomatous polyposis-coli protein or alpha-catenin. *Mol. Cell Biol.* **15**, 4819-4824. doi:10.1128/MCB.15.9.4819
- Davis, M. A., Ireton, R. C. and Reynolds, A. B. (2003). A core function for p120-catenin in cadherin turnover. *J. Cell Biol.* **163**, 525-534. doi:10.1083/jcb.200307111
- De Vries, W. N., Evsikov, A. V., Haac, B. E., Fancher, K. S., Holbrook, A. E., Kemler, R., Solter, D. and Knowles, B. B. (2004). Maternal beta-catenin and E-cadherin in mouse development. *Development* **131**, 4435-4445. doi:10.1242/dev.01316
- Derksen, P. W. B. and van de Ven, R. A. H. (2017). Shared mechanisms regulate spatiotemporal RhoA-dependent actomyosin contractility during adhesion and cell division. *Small GTPases* **1-9**.
- Donaldson, J. G. and Jackson, C. L. (2011). ARF family G proteins and their regulators: roles in membrane transport, development and disease. *Nat. Rev. Mol. Cell Biol.* **12**, 362-375. doi:10.1038/nrm3117
- Dottermusch-Heidel, C., Groth, V., Beck, L. and Önel, S. F. (2012). The Arf-GEF Shizoloner regulates N-cadherin to induce fusion competence of *Drosophila* myoblasts. *Dev. Biol.* **368**, 18-27. doi:10.1016/j.ydbio.2012.04.031
- Duda, M., Kirkland, N. J., Khalilgharibi, N., Tozluoglu, M., Yuen, A. C., Carpi, N., Bove, A., Piel, M., Charras, G., Baum, B. et al. (2019). Polarization of Myosin II refines tissue material properties to buffer mechanical stress. *Dev. Cell.* **48**, 245-260.e247.
- Ellis, S. and Mellor, H. (2000). Regulation of endocytic traffic by rho family GTPases. *Trends Cell Biol.* **10**, 85-88. doi:10.1016/S0962-8924(99)01710-9
- Fernandez-Gonzalez, R., Simoes Sde, M., Röper, J.-C., Eaton, S. and Zallen, J. A. (2009). Myosin II dynamics are regulated by tension in intercalating cells. *Dev. Cell* **17**, 736-743. doi:10.1016/j.devcel.2009.09.003
- Foty, R. A. and Steinberg, M. S. (2005). The differential adhesion hypothesis: a direct evaluation. *Dev. Biol.* **278**, 255-263. doi:10.1016/j.ydbio.2004.11.012
- Fox, D. T., Homem, C. C. F., Myster, S. H., Wang, F., Bain, E. E. and Peifer, M. (2005). Rho1 regulates *Drosophila* adherens junctions independently of p120ctn. *Development* **132**, 4819-4831. doi:10.1242/dev.02056
- Gaidarov, I., Santini, F., Warren, R. A. and Keen, J. H. (1999). Spatial control of coated-pit dynamics in living cells. *Nat. Cell Biol.* **1**, 1-7. doi:10.1038/8971
- Garrett, J. P., Lowery, A. M., Adam, A. P., Kowalczyk, A. P. and Vincent, P. A. (2017). Regulation of endothelial barrier function by p120-catenin-VE-cadherin interaction. *Mol. Biol. Cell* **28**, 85-97. doi:10.1091/mbc.e16-08-0616
- Gomez, J. M., Chumakova, L., Bulgakova, N. A. and Brown, N. H. (2016). Microtubule organization is determined by the shape of epithelial cells. *Nat. Commun.* **7**, 13172. doi:10.1038/ncomms13172
- Gul, I. S., Hulpiau, P., Saeys, Y. and van Roy, F. (2017). Evolution and diversity of cadherins and catenins. *Exp. Cell Res.* **358**, 3-9. doi:10.1016/j.yexcr.2017.03.001
- Hatzfeld, M. (2005). The p120 family of cell adhesion molecules. *Eur. J. Cell Biol.* **84**, 205-214. doi:10.1016/j.ejcb.2004.12.016
- Hayashi, T. and Carthew, R. W. (2004). Surface mechanics mediate pattern formation in the developing retina. *Nature* **431**, 647-652. doi:10.1038/nature02952
- Hirano, M., Neff, D. and Collier, S. (2009). Cell shape and epithelial patterning in the *Drosophila* embryonic epidermis. *Fly* **3**, 185-191. doi:10.4161/fly.3.3.9138
- Ho, C., Zhou, J. H., Medina, M., Goto, T., Jacobson, M., Bhidé, P. G. and Kosik, K. S. (2000). Delta-catenin is a nervous system-specific adherens junction protein which undergoes dynamic relocalization during development. *J. Comp. Neurol.* **420**, 261-276. doi:10.1002/(SICI)1096-9861(20000501)420:2<261::AID-CNE8>3.0.CO;2-Q
- Huang, J., Zhou, W. K., Dong, W., Watson, A. M. and Hong, Y. (2009). Directed, efficient, and versatile modifications of the *Drosophila* genome by genomic engineering. *Proc. Natl Acad. Sci. USA* **106**, 8284-8289. doi:10.1073/pnas.0900641106
- Humphreys, D., Liu, T., Davidson, A. C., Hume, P. J. and Koronakis, V. (2012). The *Drosophila* Arf1 homologue Arf79F is essential for lamellipodium formation. *J. Cell Sci.* **125**, 5630-5635. doi:10.1242/jcs.108092
- Humphreys, D., Davidson, A. C., Hume, P. J., Makin, L. E. and Koronakis, V. (2013). Arf6 coordinates actin assembly through the WAVE complex, a mechanism usurped by Salmonella to invade host cells. *Proc. Natl Acad. Sci. USA* **110**, 16880-16885. doi:10.1073/pnas.1311680110
- Hunter, M. V., Lee, D. M., Harris, T. J. C. and Fernandez-Gonzalez, R. (2015). Polarized E-cadherin endocytosis directs actomyosin remodeling during embryonic wound repair. *J. Cell Biol.* **210**, 801-816. doi:10.1083/jcb.201501076
- Ireton, R. C., Davis, M. A., van Hengel, J., Mariner, D. J., Barnes, K., Thoreson, M. A., Anastasiadis, P. Z., Matrisian, L., Bundy, L. M., Sealy, L. et al. (2002). A novel role for p120 catenin in E-cadherin function. *J. Cell Biol.* **159**, 465-476. doi:10.1083/jcb.200205115
- Ishiyama, N., Lee, S.-H., Liu, S., Li, G.-Y., Smith, M. J., Reichardt, L. F. and Ikura, M. (2010). Dynamic and static interactions between p120 catenin and E-cadherin regulate the stability of cell-cell adhesion. *Cell* **141**, 117-128. doi:10.1016/j.cell.2010.01.017

- Israely, I., Costa, R. M., Xie, C. W., Silva, A. J., Kosik, K. S. and Liu, X. (2004). Deletion of the neuron-specific protein delta-catenin leads to severe cognitive and synaptic dysfunction. *Curr. Biol.* **14**, 1657-1663. doi:10.1016/j.cub.2004.08.065
- Iyer, K. V., Piscitello-Gomez, R., Pajmians, J., Julicher, F. and Eaton, S. (2019). Epithelial viscoelasticity is regulated by mechanosensitive E-cadherin turnover. *Curr. Biol.* **29**, 578-591.E5.
- Jian, X. Y., Cavenagh, M., Gruschus, J. M., Randazzo, P. A. and Kahn, R. A. (2010). Modifications to the C-terminus of Arf1 alter cell functions and protein interactions. *Traffic* **11**, 732-742. doi:10.1111/j.1600-0854.2010.01054.x
- Kaksonen, M. and Roux, A. (2018). Mechanisms of clathrin-mediated endocytosis. *Nat. Rev. Mol. Cell Biol.* **19**, 313-326. doi:10.1038/nrm.2017.132
- Kawano, Y., Fukata, Y., Oshiro, N., Amano, M., Nakamura, T., Ito, M., Matsumura, F., Inagaki, M. and Kaibuchi, K. (1999). Phosphorylation of myosin-binding subunit (MBS) of myosin phosphatase by Rho-kinase in vivo. *J. Cell Biol.* **147**, 1023-1037. doi:10.1083/jcb.147.5.1023
- Kochubey, O., Majumdar, A. and Klingauf, J. (2006). Imaging clathrin dynamics in *Drosophila melanogaster* hemocytes reveals a role for actin in vesicle fission. *Traffic* **7**, 1614-1627. doi:10.1111/j.1600-0854.2006.00492.x
- Kowalczyk, A. P. and Nanes, B. A. (2012). Adherens junction turnover: regulating adhesion through cadherin endocytosis, degradation, and recycling. *Subcell. Biochem.* **60**, 197-222. doi:10.1007/978-94-007-4186-7_9
- Kumari, S. and Mayor, S. (2008). ARF1 is directly involved in dynamin-independent endocytosis. *Nat. Cell Biol.* **10**, 30-41. doi:10.1038/ncb1666
- Kureishi, Y., Kobayashi, S., Amano, M., Kimura, K., Kanaide, H., Nakano, T., Kaibuchi, K. and Ito, M. (1997). Rho-associated kinase directly induces smooth muscle contraction through myosin light chain phosphorylation. *J. Biol. Chem.* **272**, 12257-12260. doi:10.1074/jbc.272.19.12257
- Lang, R. A., Herman, K., Reynolds, A. B., Hildebrand, J. D. and Plegeman, T. F. (2014). p120-catenin-dependent junctional recruitment of Shroom3 is required for apical constriction during lens pit morphogenesis. *Development* **141**, 3177-3187. doi:10.1242/dev.107433
- Latorre, E., Kale, S., Casares, L., Gómez-González, M., Uroz, M., Valon, L., Nair, R. V., Garreta, E., Montserrat, N., Del Campo, A. et al. (2018). Active superelasticity in three-dimensional epithelia of controlled shape. *Nature* **563**, 203-208. doi:10.1038/s41586-018-0671-4
- Lecuit, T. and Lenne, P.-F. (2007). Cell surface mechanics and the control of cell shape, tissue patterns and morphogenesis. *Nat. Rev. Mol. Cell Biol.* **8**, 633-644. doi:10.1038/nrm2222
- Lee, D. M. and Harris, T. J. C. (2013). An Arf-GEF regulates antagonism between endocytosis and the cytoskeleton for *Drosophila* blastoderm development. *Curr. Biol.* **23**, 2110-2120. doi:10.1016/j.cub.2013.08.058
- Leung, T., Manser, E., Tan, L. and Lim, L. (1995). A novel serine/threonine kinase binding the Ras-related Rho Gtpase which translocates the kinase to peripheral membranes. *J. Biol. Chem.* **270**, 29051-29054. doi:10.1074/jbc.270.49.29051
- Levayer, R., Pelissier-Monier, A. and Lecuit, T. (2011). Spatial regulation of Dia and Myosin-II by RhoGEF2 controls initiation of E-cadherin endocytosis during epithelial morphogenesis. *Nat. Cell Biol.* **13**, 529-540. doi:10.1038/ncb2224
- Liang, X., Michael, M. and Gomez, G. A. (2016). Measurement of mechanical tension at cell-cell junctions using two-photon laser ablation. *Bio-protocol* **6**.
- Loerke, D., Wiensisch, M., Kochubey, O. and Klingauf, J. (2005). Differential control of clathrin subunit dynamics measured with EW-FRAP microscopy. *Traffic* **6**, 918-929. doi:10.1111/j.1600-0854.2005.00329.x
- Luchsinger, C., Aguilar, M., Burgos, P. V., Ehrenfeld, P. and Mardones, G. A. (2018). Functional disruption of the golgi apparatus protein ARF1 sensitizes MDA-MB-231 breast cancer cells to the antitumor drugs actinomycin D and vinblastine through ERK and AKT signaling. *PLoS ONE* **13**.
- Magie, C. R., Pinto-Santini, D. and Parkhurst, S. M. (2002). Rho1 interacts with p120ctn and alpha-catenin, and regulates cadherin-based adherens junction components in *Drosophila*. *Development* **129**, 3771-3782.
- Mao, Y. L., Tournier, A. L., Hoppe, A., Kester, L., Thompson, B. J. and Tapon, N. (2013). Differential proliferation rates generate patterns of mechanical tension that orient tissue growth. *EMBO J.* **32**, 2790-2803. doi:10.1038/emboj.2013.197
- McCleery, W. T., Veldhuis, J., Bennett, M. E., Lynch, H. E., Ma, X., Brodland, G. W. and Hutson, M. S. (2019). Elongated cells drive morphogenesis in a surface-wrapped finite-element model of germband retraction. *Biophys. J.* **117**, 157-169. doi:10.1016/j.bpj.2019.05.023
- McMahon, H. T. and Boucrot, E. (2011). Molecular mechanism and physiological functions of clathrin-mediated endocytosis. *Nat. Rev. Mol. Cell Biol.* **12**, 517-533. doi:10.1038/nrm3151
- Munjal, A., Philippe, J. M., Munro, E. and Lecuit, T. (2015). A self-organized biomechanical network drives shape changes during tissue morphogenesis. *Nature* **524**, 351-355. doi:10.1038/nature14603
- Myster, S. H., Cavallo, R., Anderson, C. T., Fox, D. T. and Peifer, M. (2003). *Drosophila* p120catenin plays a supporting role in cell adhesion but is not an essential adherens junction component. *J. Cell Biol.* **160**, 433-449. doi:10.1083/jcb.200211083
- Nanes, B. A., Chiasson-MacKenzie, C., Lowery, A. M., Ishiyama, N., Faundez, V., Ikura, M., Vincent, P. A. and Kowalczyk, A. P. (2012). p120-catenin binding masks an endocytic signal conserved in classical cadherins. *J. Cell Biol.* **199**, 365-380. doi:10.1083/jcb.201205029
- Nestor-Bergmann, A., Stooke-Vaughan, G. A., Goddard, G. K., Starborg, T., Jensen, O. E. and Woolner, S. (2019). Decoupling the roles of cell shape and mechanical stress in orienting and cueing epithelial mitosis. *Cell Rep.* **26**, 2088-2100.e4.
- Oas, R. G., Nanes, B. A., Esimai, C. C., Vincent, P. A., Garcia, A. J. and Kowalczyk, A. P. (2013). p120-catenin and beta-catenin differentially regulate cadherin adhesive function. *Mol. Biol. Cell* **24**, 704-714. doi:10.1091/mbc.e12-06-0471
- Ozawa, M., Ringwald, M. and Kemler, R. (1990). Uvomorulin catenin complex formation is regulated by a specific domain in the cytoplasmic region of the cell-adhesion molecule. *Proc. Natl Acad. Sci. USA* **87**, 4246-4250. doi:10.1073/pnas.87.11.4246
- Pacquelet, A., Lin, L. and Rørth, P. (2003). Binding site for p120/delta-catenin is not required for *Drosophila* E-cadherin function in vivo. *J. Cell Biol.* **160**, 313-319. doi:10.1083/jcb.200207160
- Padovani, D., Folly-Klan, M., Labarde, A., Boulakirba, S., Campanacci, V., Franco, M., Zeghouf, M. and Cherfils, J. (2014). EFA6 controls Arf1 and Arf6 activation through a negative feedback loop. *Proc. Natl Acad. Sci. USA* **111**, 12378-12383. doi:10.1073/pnas.1409832111
- Pettitt, J., Cox, E. A., Broadbent, I. D., Flett, A. and Hardin, J. (2003). The caenorhabditis elegans p120 catenin homologue, JAC-1, modulates cadherin-catenin function during epidermal morphogenesis. *J. Cell Biol.* **162**, 15-22. doi:10.1083/jcb.200212136
- Pilauri, V., Bewley, M., Diep, C. and Hopper, J. (2005). Gal80 dimerization and the yeast GAL gene switch. *Genetics* **169**, 1903-1914. doi:10.1534/genetics.104.036723
- Priya, R., Yap, A. S. and Gomez, G. A. (2013). E-cadherin supports steady-state Rho signaling at the epithelial zonula adherens. *Differentiation* **86**, 133-140. doi:10.1016/j.diff.2013.01.002
- Priya, R., Gomez, G. A., Budnar, S., Verma, S., Cox, H. L., Hamilton, N. A. and Yap, A. S. (2015). Feedback regulation through myosin II confers robustness on RhoA signalling at E-cadherin junctions. *Nat. Cell Biol.* **17**, 1282-1293.
- Ratheesh, A., Gomez, G. A., Priya, R., Verma, S., Kovacs, E. M., Jiang, K., Brown, N. H., Akhmanova, A., Stehbens, S. J. and Yap, A. S. (2012). Centralspindlin and alpha-catenin regulate Rho signalling at the epithelial zonula adherens. *Nat. Cell Biol.* **14**, 818-828. doi:10.1038/ncb2532
- Reynolds, A. B. (2007). p120-catenin: past and present. *Biochim. Biophys. Acta* **1773**, 2-7. doi:10.1016/j.bbamcr.2006.09.019
- Riedl, J., Crevenna, A. H., Kessenbrock, K., Yu, J. H., Neukirchen, D., Bista, M., Bradke, F., Jenne, D., Holak, T. A., Werb, Z. et al. (2008). Lifeact: a versatile marker to visualize F-actin. *Nat. Methods* **5**, 605-607. doi:10.1038/nmeth.1220
- Rodrigues, F. F., Shao, W. and Harris, T. J. C. (2016). The Arf GAP Asap promotes Arf1 function at the golgi for cleavage furrow biosynthesis in *Drosophila*. *Mol. Biol. Cell* **27**, 3143-3155. doi:10.1091/mbc.e16-05-0272
- Rouhana, J., Padilla, A., Estaran, S., Bakari, S., Delbecq, S., Boublik, Y., Chopineau, J., Pugnère, M. and Chavanieu, A. (2013). Kinetics of interaction between ADP-ribosylation factor-1 (Arf1) and the Sec7 domain of Arno guanine nucleotide exchange factor, modulation by allosteric factors, and the uncompetitive inhibitor brefeldin A. *J. Biol. Chem.* **288**, 4659-4672. doi:10.1074/jbc.M112.391748
- Sato, K., Watanabe, T., Wang, S. J., Kakeno, M., Matsuzawa, K., Matsui, T., Yokoi, K., Murase, K., Sugiyama, I., Ozawa, M. et al. (2011). Numb controls E-cadherin endocytosis through p120 catenin with aPKC. *Mol. Biol. Cell* **22**, 3103-3119. doi:10.1091/mbc.e11-03-0274
- Saye, R. (2017). Implicit mesh discontinuous Galerkin methods and interfacial gauge methods for high-order accurate interface dynamics, with applications to surface tension dynamics, rigid body fluid-structure interaction, and free surface flow: part II. *J. Comput. Phys.* **344**, 683-723. doi:10.1016/j.jcp.2017.05.003
- Scarpa, E., Finet, C., Blanchard, G. B. and Sanson, B. (2018). Actomyosin-driven tension at compartmental boundaries orients cell division independently of cell geometry in vivo. *Dev. Cell* **47**, 727-740.e6.
- Shao, W., Wu, J., Chen, J., Lee, D. M., Tishkina, A. and Harris, T. J. C. (2010). A modifier screen for Bazooka/Par-3 interacting genes in the *Drosophila* embryo epithelium. *PLoS ONE* **5**.
- Shapiro, L. and Weis, W. I. (2009). Structure and biochemistry of cadherins and catenins. *CSH Perspect. Biol.* **1**.
- Shibamoto, S., Hayakawa, M., Takeuchi, K., Hori, T., Miyazawa, K., Kitamura, N., Johnson, K. R., Wheelock, M. J., Matsuyoshi, N., Takeichi, M. et al. (1995). Association of P120, a tyrosine kinase substrate, with E-cadherin/catenin complexes. *J. Cell Biol.* **128**, 949-957. doi:10.1083/jcb.128.5.949
- Simões, S. D., Blankenship, J. T., Weitz, O., Farrell, D. L., Tamada, M., Fernandez-Gonzalez, R. and Zallen, J. A. (2010). Rho-kinase directs Bazooka/Par-3 planar polarity during *Drosophila* axis elongation. *Dev. Cell* **19**, 377-388. doi:10.1016/j.devcel.2010.08.011
- Singh, V., Davidson, A. C., Hume, P. J., Humphreys, D. and Koronakis, V. (2017). Arf GTPase interplay with Rho GTPases in regulation of the actin cytoskeleton. *Small GTPases* **4**, 411-418.
- Spiering, D. and Hodgson, L. (2011). Dynamics of the Rho-family small GTPases in actin regulation and motility. *Cell Adh. Migr.* **5**, 170-180. doi:10.4161/cam.5.2.14403

- Sugimura, K., Lenne, P.-F. and Graner, F. (2016). Measuring forces and stresses in situ in living tissues. *Development* **143**, 186–196. doi:10.1242/dev.119776
- Takeichi, M. (1977). Functional correlation between cell adhesive properties and some cell-surface proteins. *J. Cell Biol.* **75**, 464–474. doi:10.1083/jcb.75.2.464
- Taulet, N., Comunale, F., Favard, C., Charrasse, S., Bodin, S. and Gauthier-Rouvière, C. (2009). N-cadherin/p120 catenin association at cell-cell contacts occurs in cholesterol-rich membrane domains and is required for RhoA activation and myogenesis. *J. Biol. Chem.* **284**, 23137–23145. doi:10.1074/jbc.M109.017665
- Tepass, U. and Hartenstein, V. (1994). The development of cellular junctions in the *Drosophila* embryo. *Dev. Biol.* **161**, 563–596. doi:10.1006/dbio.1994.1054
- Toret, C. P., D'Ambrosio, M. V., Vale, R. D., Simon, M. A. and Nelson, W. J. (2014). A genome-wide screen identifies conserved protein hubs required for cadherin-mediated cell-cell adhesion. *J. Cell Biol.* **204**, 265–279. doi:10.1083/jcb.201306082
- Trojanovsky, R. B., Sokolov, E. P. and Trojanovsky, S. M. (2006). Endocytosis of cadherin from intracellular junctions is the driving force for cadherin adhesive dimer disassembly. *Mol. Biol. Cell* **17**, 3484–3493. doi:10.1091/mbc.e06-03-0190
- van Roy, F. and Berx, G. (2008). The cell-cell adhesion molecule E-cadherin. *Cell. Mol. Life Sci.* **65**, 3756–3788. doi:10.1007/s00018-008-8281-1
- Winklbauer, R. (2015). Cell adhesion strength from cortical tension - an integration of concepts. *J. Cell Sci.* **128**, 3687–3693. doi:10.1242/jcs.174623
- Wu, X., Zhao, X., Baylor, L., Kaushal, S., Eisenberg, E. and Greene, L. E. (2001a). Clathrin exchange during clathrin-mediated endocytosis. *J. Cell Biol.* **155**, 291–300. doi:10.1083/jcb.200104085
- Wu, X. F., Zhao, X. H., Kaushal, S., Baylor, L., Eisenberg, E. and Greene, L. (2001b). Clathrin exchange during clathrin mediated endocytosis. *J. Cell Biol.* **155**, 291–300. doi:10.1083/jcb.200104085
- Wyatt, T. P. J., Fouchard, J., Lisica, A., Khalilgharibi, N., Baum, B., Recho, P., Kabla, A. J. and Charas, G. T. (2020). Actomyosin controls planarity and folding of epithelia in response to compression. *Nat. Mater.* **19**, 109–117. doi:10.1038/s41563-019-0461-x
- Xiao, K. Y., Allison, D. F., Buckley, K. M., Kottke, M. D., Vincent, P. A., Faundez, V. and Kowalczyk, A. P. (2003). Cellular levels of p120 catenin function as a set point for cadherin expression levels in microvascular endothelial cells. *J. Cell Biol.* **163**, 535–545. doi:10.1083/jcb.200306001
- Yao, M., Qiu, W., Liu, R., Efremov, A. K., Cong, P., Seddiki, R., Payre, M., Lim, C. T., Ladoux, B., Mège, R.-M. et al. (2014). Force-dependent conformational switch of alpha-catenin controls vinculin binding. *Nat. Commun.* **5**, 4525. doi:10.1038/ncomms5525
- Yap, A. S., Niessen, C. M. and Gumbiner, B. M. (1998). The juxtamembrane region of the cadherin cytoplasmic tail supports lateral clustering, adhesive strengthening, and interaction with p120ctn. *J. Cell Biol.* **141**, 779–789. doi:10.1083/jcb.141.3.779
- Yu, J. C. and Fernandez-Gonzalez, R. (2016). Local mechanical forces promote polarized junctional assembly and axis elongation in *Drosophila*. *eLife* **5**, doi:10.7554/eLife.10757
- Yu, H. H., Dohn, M. R., Markham, N. O., Coffey, R. J. and Reynolds, A. B. (2016). p120-catenin controls contractility along the vertical axis of epithelial lateral membranes. *J. Cell Sci.* **129**, 80–94. doi:10.1242/jcs.177550
- Zebda, N., Tian, Y. F., Tian, X. Y., Gawlak, G., Higginbotham, K., Reynolds, A. B., Birukova, A. A. and Birukov, K. G. (2013). Interaction of p190RhoGAP with C-terminal domain of p120-catenin modulates endothelial cytoskeleton and permeability. *J. Biol. Chem.* **288**, 18290–18299. doi:10.1074/jbc.M112.432757